

AD-A106 060

AD *A-106060*

TECHNICAL REPORT ARBRL-TR-02363

NUMERICAL SIMULATION OF STEADY SUPERSONIC  
FLOW OVER AN OGIVE CYLINDER  
BOATTAIL BODY

Lewis B. Schiff  
Walter B. Sturek

September 1981



**US ARMY ARMAMENT RESEARCH AND DEVELOPMENT COMMAND**  
**BALLISTIC RESEARCH LABORATORY**  
**ABERDEEN PROVING GROUND, MARYLAND**

Approved for public release; distribution unlimited.

Destroy this report when it is no longer needed.  
Do not return it to the originator.

Secondary distribution of this report by originating  
or sponsoring activity is prohibited.

Additional copies of this report may be obtained  
from the National Technical Information Service,  
U.S. Department of Commerce, Springfield, Virginia  
22151.

The findings in this report are not to be construed as  
an official Department of the Army position, unless  
so designated by other authorized documents.

*The use of trade names or manufacturers' names in this report  
does not constitute indorsement of any commercial product.*

UNCLASSIFIED

SECURITY CLASSIFICATION OF THIS PAGE (When Data Entered)

REPORT DOCUMENTATION PAGE		READ INSTRUCTIONS BEFORE COMPLETING FORM
1. REPORT NUMBER TECHNICAL REPORT ARBRL-TR-02363	2. GOVT ACCESSION NO.	3. RECIPIENT'S CATALOG NUMBER
4. TITLE (and Subtitle) NUMERICAL SIMULATION OF STEADY SUPERSONIC FLOW OVER AN OGIVE CYLINDER BOATTAIL BODY		5. TYPE OF REPORT & PERIOD COVERED Final
		6. PERFORMING ORG. REPORT NUMBER
7. AUTHOR(s) Lewis B. Schiff (NASA AMES RESEARCH CENTER) Walter B. Sturek		8. CONTRACT OR GRANT NUMBER(s)
9. PERFORMING ORGANIZATION NAME AND ADDRESS U.S. Army Ballistic Research Laboratory (ATTN: DRDAR-BLL) Aberdeen Proving Ground, Maryland 21005		10. PROGRAM ELEMENT, PROJECT, TASK AREA & WORK UNIT NUMBERS 1L161102AH43
11. CONTROLLING OFFICE NAME AND ADDRESS U.S. Army Armament Research & Development Command U.S. Army Ballistic Research Laboratory (ATTN: DRDAR-BL) Aberdeen Proving Ground, MD 21005		12. REPORT DATE SEPTEMBER 1981
		13. NUMBER OF PAGES 47
14. MONITORING AGENCY NAME & ADDRESS (if different from Controlling Office)		15. SECURITY CLASS. (of this report) Unclassified
		15a. DECLASSIFICATION/DOWNGRADING SCHEDULE
16. DISTRIBUTION STATEMENT (of this Report) Approved for public release, distribution unlimited.		
17. DISTRIBUTION STATEMENT (of the abstract entered in Block 20, if different from Report)		
18. SUPPLEMENTARY NOTES		
19. KEY WORDS (Continue on reverse side if necessary and identify by block number) Supersonic Flow Turbulent viscous flow Parabolized Navier-Stokes Three dimensional flow		
20. ABSTRACT (Continue on reverse side if necessary and identify by block number) A recently reported Parabolized Navier-Stokes code has been employed to compute the supersonic flow field surrounding an ogive-cylinder-boattail body at incidence. The computations were performed for flow conditions where an extensive series of experimental surface pressure and turbulent boundary-layer profile measurements had been obtained. Comparison between the computational results and experimental measurements for angles of attack up to 6° show excellent agreement. At angles greater than 6° discrepancies are observed which are tentatively attributed to three-dimensional turbulence modeling errors.		

UNCLASSIFIED

## TABLE OF CONTENTS

	<u>Page</u>
LIST OF ILLUSTRATIONS.....	5
I. INTRODUCTION.....	7
II. GOVERNING EQUATIONS AND NUMERICAL SCHEME.....	7
III. CONICAL INITIAL SOLUTIONS.....	11
IV. RESULTS.....	11
A. Model Geometry and Experimental Measurements.....	11
B. PNS Computations and Code Performance.....	12
C. Comparison Between Computation and Experiment.....	13
V. CONCLUDING REMARKS.....	16
REFERENCES.....	17
LIST OF SYMBOLS.....	43
DISTRIBUTION LIST.....	45

## LIST OF ILLUSTRATIONS

<u>Figure</u>		<u>Page</u>
1	Coordinates and Notation.....	19
2	Subsonic Layer Approximation.....	20
3	Circumferential Surface Pressure Distribution on 10° Cone; M = 3.0, $\alpha = 2.0^\circ$ , $Re_x = 1.54 \times 10^6$ .....	21
4	Windward and Leeward Boundary-Layer Velocity Profiles on 10° Cone; M = 3.0, $\alpha = 2.0^\circ$ , $Re_x = 1.54 \times 10^6$ .....	22
5	Ogive-Cylinder-Boattail Model Dimensions.....	23
6	Axial Surface Pressure Distribution on Ogive-Cylinder-Boattail Body; M = 3.0, $\alpha = 4.2^\circ$ , $Re_\infty = 2.13 \times 10^7/m$ .....	24
7	Axial Surface Pressure Distribution on Ogive-Cylinder-Boattail Body; M = 3.0, $\alpha = 6.3^\circ$ , $Re_\infty = 2.13 \times 10^7/m$ .....	25
8	Axial Surface Pressure Distribution on Ogive-Cylinder-Boattail Body; M = 3.0, $\alpha = 10.4^\circ$ , $Re_\infty = 2.13 \times 10^7/m$ .....	26
9	Circumferential Surface Pressure Distributions; M = 3.0, $\alpha = 6.3^\circ$ , $Re_\infty = 2.13 \times 10^7/m$ .....	27
	a. x = 279mm (0.915 ft), Cylinder.....	27
	b. x = 330mm (1.082 ft), Boattail.....	28
10	Circumferential Surface Pressure Distributions; M = 3.0, $\alpha = 10.4^\circ$ , $Re_\infty = 2.13 \times 10^7/m$ .....	29
	a. x = 279mm (0.915 ft), Cylinder.....	29
	b. x = 330mm (1.082 ft), Boattail.....	30
11	Circumferential Skin Friction Coefficient Distribution, M = 3.0, x = 254mm, $Re_x = 5.41 \times 10^6$ .....	31
12	Boundary-Layer Velocity Profiles on Ogive-Cylinder-Boattail Body; M = 3.0, $\alpha = 4.2^\circ$ , $Re_\infty = 2.13 \times 10^7/m$ , x = 254mm (0.833 ft), Cylinder.....	32
13	Boundary-Layer Velocity Profiles on Ogive-Cylinder-Boattail Body; M = 3.0, $\alpha = 4.2^\circ$ , $Re_\infty = 2.13 \times 10^7/m$ , x = 324mm (1.063 ft), Boattail.....	33
14	Boundary-Layer Velocity Profiles on Ogive-Cylinder-Boattail Body; M = 3.0, $\alpha = 6.3^\circ$ , $Re_\infty = 2.13 \times 10^7/m$ , x = 254mm (0.833 ft), Cylinder.....	34

LIST OF ILLUSTRATIONS  
(Continued)

<u>Figure</u>		<u>Page</u>
15	Boundary-Layer Velocity Profiles on Ogive-Cylinder-Boattail Body; $M = 3.0$ , $\alpha = 6.3^\circ$ , $Re_\infty = 2.13 \times 10^7/m$ , $x = 324mm$ (1.063 ft), Boattail.....	35
16	Boundary-Layer Velocity Profiles on Ogive-Cylinder Body; $M = 3.0$ , $\alpha = 6.3^\circ$ , $Re_\infty = 2.13 \times 10^7/m$ , $x = 318mm$ (1.043 ft).....	36
17	Crossflow Plane Velocity Vectors on Boattail; $M = 3.0$ , $\alpha = 4.2^\circ$ , $Re_\infty = 2.13 \times 10^7/m$ , $x = 324mm$ (1.063 ft).....	37
18	Crossflow Plane Velocity Vectors on Boattail; $M = 3.0$ , $\alpha = 6.3^\circ$ , $Re_\infty = 2.13 \times 10^7/m$ , $x = 324mm$ (1.063 ft).....	38
19	Crossflow Plane Velocity Vectors on Boattail; $M = 3.0$ , $\alpha = 10.4^\circ$ , $Re_\infty = 2.13 \times 10^7/m$ , $x = 324mm$ (1.063 ft).....	39
20	Vapor-Screen Flow Visualization on Boattail; $M = 3.0$ , $\alpha = 4.2^\circ$ , $Re_\infty = 2.13 \times 10^7/m$ .....	40
21	Vapor-Screen Flow Visualization on Boattail; $M = 3.0$ , $\alpha = 6.3^\circ$ , $Re_\infty = 2.13 \times 10^7/m$ .....	41
22	Vapor-Screen Flow Visualization on Boattail; $M = 3.0$ , $\alpha = 10.4^\circ$ , $Re_\infty = 2.13 \times 10^7/m$ .....	42

## I. INTRODUCTION

The use of separate codes for computing the inviscid flow and turbulent boundary-layer development over yawed bodies of revolution has yielded some very good solutions for cone and ogive-cylinder shapes<sup>1</sup>. However, the authors have found that application of these techniques to bodies with boattail afterbodies has not yielded satisfactory results even at small angle of attack ( $\alpha < 4^\circ$ ).

Several recent publications have reported supersonic flow-field computations using Parabolized Navier-Stokes (PNS) techniques. These publications have reported very good results for cone models for laminar and turbulent viscous flow<sup>2,3,4</sup>, and for ogive-cylinder bodies and laminar viscous flow<sup>4</sup>. The PNS method appears to offer an attractive technique for computing flow over bodies with discontinuities in surface curvature (such as occurs at the junction between the cylinder and the boattail) since the inviscid flow and viscous layer are computed simultaneously. Further, the PNS method permits adequate flow-field resolution to be achieved with very reasonable computer costs. This report describes the results of detailed comparisons of PNS computational results to experimental measurements for surface pressures and turbulent boundary-layer profile characteristics of an ogive-cylinder-boattail body at Mach = 3 and angles of attack up to  $10^\circ$ . The PNS code used is that reported by Schiff and Steger<sup>5</sup>.

## II. GOVERNING EQUATIONS AND NUMERICAL SCHEME

A body-conforming  $\xi, \eta, \zeta$ , coordinate system (Figure 1) is used which maps the body surface and outer boundary of the flow region in physical space onto coordinate surfaces of the computational space. This transformation

- 
1. Sturek, W. B., Dwyer, H. A., Kayser, L. D., Nietubicz, C. J., Reklis, R. P., and Opalka, K. D., "Computations of Magnus Effects for a Yawed, Spinning Body of Revolution," AIAA Journal, Vol 16, No. 7, July 1978, pp. 687-692.
  2. Lin, T. C., and Rubin, S. G., "Viscous Flow Over a Cone at Moderate Incidence: I-Hypersonic Tip Region," International Journal of Computers and Fluids, Vol 1, 1973, pp. 37-57.
  3. Lubard, S. C., and Helliwell, W. S., "Calculation of the Flow on a Cone at High Angle of Attack," AIAA Journal, Vol 12, July 1974, pp. 965-974.
  4. Rakich, J. V., Vigneron, Y. C., and Agarwal, R., "Computation of Supersonic Viscous Flows Over Ogive-Cylinders at Angle of Attack," AIAA Paper No. 79-0131, 17th Aerospace Sciences Meeting, January 1979.
  5. Schiff, L. B., and Steger, J. L., "Numerical Simulation of Steady Supersonic Viscous Flow," AIAA Journal, Vol. 18, No. 12, December 1980, pp. 1421-1430.

simplifies the application of surface boundary conditions and permits the approximation of neglecting streamwise and circumferential viscous terms in high-Reynolds-number flow (see Reference 5). The resulting steady thin-layer PNS equations can be written in strong conservation-law form in terms of nondimensional variables (Reference 5) as

$$\frac{\partial \hat{E}_s}{\partial \xi} + \frac{\partial \hat{F}}{\partial \eta} + \frac{\partial \hat{G}}{\partial \zeta} = \frac{1}{\text{Re}} \frac{\partial \hat{S}}{\partial \zeta} \quad (1)$$

where

$\xi = \xi(x)$  is the axial (marching) coordinate  
 $\eta = \eta(x,y,z)$  is the circumferential coordinate  
 $\zeta = \zeta(x,y,z)$  is the normal coordinate

The inviscid flux vectors in Eq. (1) are

$$\hat{E}_s = J^{-1} \begin{bmatrix} \rho U \\ \rho U U + \xi_x p \\ \rho V U \\ \rho W U \\ (e+p_s)U \end{bmatrix}, \quad F = J^{-1} \begin{bmatrix} \rho V \\ \rho U V + \eta_x p \\ \rho V V + \eta_y p \\ \rho W V + \eta_z p \\ (e+p)V \end{bmatrix}, \quad G = J^{-1} \begin{bmatrix} \rho W \\ \rho U W + \zeta_x p \\ \rho V W + \zeta_y p \\ \rho W W + \zeta_z p \\ (e+p)W \end{bmatrix} \quad (2)$$

with contravariant velocity components

$$\begin{aligned} U &= \xi_x u \\ V &= \eta_x u + \eta_y v + \eta_z w \\ W &= \zeta_x u + \zeta_y v + \zeta_z w \end{aligned} \quad (3)$$

The internal energy of the gas  $e_i$  is defined in terms of the conservative variables as

$$e_i = (e/\rho) - 0.5(u^2 + v^2 + w^2) \quad (4)$$

while the equation of state for a perfect gas with ratio of specific heats  $\gamma$  is

$$p/\rho = (\gamma - 1)e_i = a^2/\gamma \quad (5)$$

Variations of body geometry are included in Eqs. (1)-(3) through the presence of metric terms  $\xi_x, \eta_x, \eta_y$ , etc., and the Jacobian of the transformation  $J$ , which appears in the flux vector.

The thin-layer-model viscous terms, valid for high-Reynolds-number flow and body-conforming coordinates are

$$\hat{S} = J^{-1} \begin{bmatrix} 0 \\ \mu(\zeta_x^2 + \zeta_y^2 + \zeta_z^2)u_\zeta + (\mu/3)(\zeta_x u_\zeta + \zeta_y v_\zeta + \zeta_z w_\zeta)\zeta_x \\ \mu(\zeta_x^2 + \zeta_y^2 + \zeta_z^2)v_\zeta + (\mu/3)(\zeta_x u_\zeta + \zeta_y v_\zeta + \zeta_z w_\zeta)\zeta_y \\ \mu(\zeta_x^2 + \zeta_y^2 + \zeta_z^2)w_\zeta + (\mu/3)(\zeta_x u_\zeta + \zeta_y v_\zeta + \zeta_z w_\zeta)\zeta_z \\ \{(\zeta_x^2 + \zeta_y^2 + \zeta_z^2)[(\mu/2)(u^2 + v^2 + w^2)_\zeta \\ + \kappa Pr^{-1}(\gamma-1)^{-1}(a^2)_\zeta] + (\mu/3)(\zeta_x u \\ + \zeta_y v + \zeta_z w)(\zeta_x u_\zeta + \zeta_y v_\zeta + \zeta_z w_\zeta)\} \end{bmatrix} \quad (6)$$

For turbulent flow computations the coefficient of molecular viscosity ( $\mu$ ) and thermal conductivity ( $\kappa$ ) appearing in Eq. (6) are computed using the two-layer Cebeci-type eddy viscosity model reported by Baldwin and Lomax<sup>6</sup>. The various constants within the model were set to the values suggested in Reference 6, with the exception that the turbulent Prandtl number  $Pr_t$  was set to 0.8.

Equation (1) is parabolic-like with respect to  $\xi$ , and can thus be marched downstream in the  $\xi$  direction from an initial data plane (subject to appropriate body and free-stream boundary conditions), under those conditions where the local flow is supersonic. By evaluating the pressure,  $p_s$ , which appears in the  $\hat{E}_s$  flux vector using the subsonic layer approximation, Eq. (1) can be kept stable for marching for subsonic points as well. If  $p_s$  is set equal to the local pressure for supersonic points, and is evaluated from  $\partial p_s / \partial \zeta = 0$  (Figure 2) for points within the subsonic viscous layer adjacent to a wall, Eq. (1) can be stably marched for all flows where  $U > 0$ ; that is, for flows without streamwise reversal (see Reference 5 for associated stability analysis).

The numerical algorithm used to advance Eq. (1) downstream in  $\xi$  is a noniterative, implicit, approximately factored finite-difference scheme,

---

6. Baldwin, B. S., and Lomax, H., "Thin Layer Approximation and Algebraic Model for Separated Turbulent Flows," AIAA Paper No. 78-257, 16th Aerospace Sciences Meeting, January 1978.

analogous to the one developed by Beam and Warming<sup>7</sup> for the solution of the unsteady Navier-Stokes equations. The algorithm can be written in so-called delta form as

$$\left[ \begin{aligned}
 & [\tilde{A}_s^j + (1 - \alpha)\Delta\xi(\delta_\eta \tilde{B}^j)](\tilde{A}_s^j)^{-1} \\
 & \times [\tilde{A}_s^j + (1 - \alpha)\Delta\xi(\delta_\zeta \tilde{C}^j - \text{Re}^{-1} \delta_\zeta \tilde{M}^j)]\Delta\hat{q}^j \\
 & = -(\tilde{A}_s^j - \tilde{A}_s^{j-1})\hat{q}^j + \alpha(\hat{E}_s^j - \hat{E}_s^{j-1}) \\
 & - (1 - \alpha)\Delta\xi\{\delta_\eta[\eta_x^{j+1}(E/J)^j + \eta_y^{j+1}(F/J)^j + \eta_z^{j+1}(G/J)^j] \\
 & \quad + \delta_\zeta[\zeta_x^{j+1}(E/J)^j + \zeta_y^{j+1}(F/J)^j + \zeta_z^{j+1}(G/J)^j] \\
 & \quad - \text{Re}^{-1}\delta_\zeta \tilde{S}^j\} - [(\epsilon_x/J)^{j+1}E_p^j - (\epsilon_x/J)^j E_p^{j-1}] + \mathcal{D}\hat{q}^j
 \end{aligned} \right] \tag{7}$$

where  $\hat{q} = J^{-1} (\rho, \rho u, \rho v, \rho w, e)$

The  $\delta$ 's represent second order central difference operators while  $\Delta$  represents a conventional forward difference. The Jacobian matrices A, B, and C are defined as  $\frac{\partial E}{\partial q}$ ,  $\frac{\partial F}{\partial q}$ , and  $\frac{\partial G}{\partial q}$ , respectively. The coefficient matrix M is obtained from the Taylor series linearization of the viscous vector S. The algorithm shown in Eq. (7) is second order accurate in  $\xi$  for  $\alpha = 1/3$ , and is first order accurate in  $\xi$  for  $\alpha = 0$ . The fourth order dissipation term is represented by  $\mathcal{D}$  which is added to damp high-frequency oscillations.

The algorithm is conservative, of second-order accuracy in the marching direction, and can be either second- or fourth-order accurate in the cross-flow plane. The algorithm has been applied to compute a variety of laminar and turbulent viscous flows and the results have been in excellent agreement with those obtained from more costly time-dependent computations. Full details of the notation, of the PNS assumption and derivation of the algorithm, and the associated stability analysis and application of boundary conditions are found in Reference 5.

---

7. Beam, R., and Warming, R. F., "An Implicit Factored Scheme for the Compressible Navier-Stokes Equations," *AIAA Journal*, Vol. 16, No. 4, April 1978, pp 393-402.

### III. CONICAL INITIAL SOLUTIONS

In general, the initial data plane for the marching method must be supplied from an auxiliary computation. However, when treating the flow over conical or pointed bodies, the marching code can be used to generate its own initial data plane. As outlined in Reference 5, for inviscid conical flows, a conical grid is selected and the flow variables are initially set to free-stream values. The solution is marched downstream from an initial station and, after each step, the solution is scaled to place it back at the original station. When no change in the flow variables occur with further marching, the variables are constant along rays, and a conical solution has been generated. If the flow variables within the viscous layer can also be assumed to be locally constant along rays, the same procedure can be used to generate viscous conical solutions.

The conical viscous approximation is subject to criticism since it assumes the boundary-layer displacement thickness to vary locally linearly with distance downstream, instead of the actual  $x^{0.5}$  (laminar) or  $x^{0.8}$  (turbulent) growth. To assess the accuracy of the starting procedure, turbulent viscous solutions were generated using the conical assumption at two stations, 15.2mm and 61.0mm downstream from the apex of a  $10^\circ$  cone, at  $M_\infty = 3.0$ ,  $\alpha = 2.0^\circ$ , and  $Re = 2.53 \times 10^6/m$ . The upstream ( $x = 15.2$  mm) solution was then used as input for the marching code to obtain a marching solution for  $15.2\text{mm} < x < 61.0$  mm. The marching solution at  $x = 61.0$  mm, free from the errors of the conical approximations, are compared to the locally conical viscous flow generated at  $x = 61.0$  mm, in Figures 3-4. The circumferential surface pressure distribution is shown in Figure 3, while boundary-layer velocity profiles on the windward and leeward rays are shown in Figure 4. At these flow conditions the conical solution is virtually indistinguishable from the marching code solution, thus demonstrating the suitability of the locally conical approximation.

### IV. RESULTS

#### A. Model Geometry and Experimental Measurements.

The dimensions of the ogive-cylinder-boattail model used for this study are shown in Figure 5. The model is 6 calibers long with a 1-caliber,  $7^\circ$  boattail, and closely resembles a modern low-drag artillery projectile.

A number of wind-tunnel experiments have been conducted for this model geometry in order to obtain data for comparison to numerical computations. The data acquired include measurements of wall static pressure<sup>8</sup>, turbulent

---

8. Reklis, R. P., and Sturek, W. B., "Surface Pressure Measurements on Slender Bodies at Angle of Attack in Supersonic Flow," U.S. Army Ballistic Research Laboratory, ARRADCOM Memorandum Report ARBRL-MR-02876, Aberdeen Proving Ground, MD, November 1978. AD A064097.

boundary-layer velocity profiles<sup>9,10</sup>, surface skin friction<sup>9</sup>, aerodynamic forces, and flow visualization. The measurements of primary interest here are the wall static pressure and boundary-layer profile characteristics.

The test conditions were  $M = 3$  with a tunnel total pressure of 0.298 MPa and tunnel total temperature of 308°K. These conditions produced a free-stream Reynolds number of  $7.3 \times 10^6$  based on the model length. The boundary layer was tripped near the tip of the model to produce a reliable turbulent flow. All tests were performed using SSWT Number One at the U.S. Army Ballistic Research Laboratory. This facility, which is no longer in operation, was a continuous flow tunnel with a flexible plate nozzle. The test section size was 330 × 380mm (13 × 15 in.).

The surface pressure measurements were made using a model with a single row of 10 pressure taps along the body length. Data were obtained as a function of circumferential position by rotating the model in increments of 10°.

Boundary-layer velocity profiles were obtained from measurements of impact pressure using a flattened total head probe. Since measurements were not made of the total temperature through the boundary layer, the temperature distribution was estimated using the Crocco linear relationship.

The Preston tube technique was used to obtain measured values for wall shear stress on the cylinder portion of the model. These measurements are not expected to be more accurate than ±15% for this application; however, the data are of qualitative interest.

Further details of the experiments including tabulations of the data are available in References 8-10.

## B. PNS Computations and Code Performance

Computations were performed for a body having the same geometric shape as the experimental model, and for flow conditions duplicating that of the experiment. The tip of the ogive was replaced with a cone tangent to the ogive at

- 
9. Kayser, L. D., and Sturek, W. B., "Experimental Measurements in the Turbulent Boundary Layer of a Yawed, Spinning Ogive-Cylinder Body of Revolution at Mach 3.0. Part II. Data Tabulation", U.S. Army Ballistic Research Laboratory/ARRADCOM Memorandum Report ARBRL-MR-02813, Aberdeen Proving Ground, MD, March 1978. AD A055707.
  10. Kayser, L. D., and Sturek, W. B., "Turbulent Boundary Layer Measurements on the Boattail Section of a Yawed, Spinning Projectile Shape at Mach 3.0", U.S. Army Ballistic Research Laboratory/ARRADCOM Memorandum Report ARBRL-MR-02880, Aberdeen Proving Ground, MD, November 1978. AD A065355.

$x = 15.2\text{mm}$  (see Figure 5). Turbulent conical solutions were generated at that station and used as initial data for the PNS marching code.

The computations presented here resulted from a large number of numerical runs in which the step size, grid spacing, and smoothing constants were varied widely. The step size,  $\Delta x$ , was varied from 0.30mm to 0.76mm without significant changes being observed in the solution. The most critical variable is the grid spacing across the viscous layer. Experience has shown that adequate resolution of the viscous layer results if a value of

$y^+ \approx 5$  ( $y^+ = \rho_w U_\tau y / \mu_w$ ,  $U_\tau = \sqrt{\tau_w / \rho_w}$ ) is obtained at the first point above the body surface at all axial stations. The present computations used a grid consisting of 36 circumferential points ( $\Delta\phi = 10^\circ$ ) and 50 points radially between the body and the outer boundary. Computation time on a CDC 7600 computer is 2.3 sec/step with this size grid.

### C. Comparison Between Computation and Experiment

1. Surface Pressure. The PNS computations are compared to experimental measurements, and to inviscid flow computations made using codes<sup>11,12</sup> based on MacCormack's predictor-corrector technique (Figures 6-10). Longitudinal surface pressure distributions along the windward and leeward rays are shown in Figures 6-8 for angles of attack of  $4.2^\circ$ ,  $6.3^\circ$ , and  $10.4^\circ$ , respectively. The PNS and inviscid computations are both in excellent agreement with the experimental measurements for angles of attack up to  $4.2^\circ$ . However, it is of interest to note that the PNS computations exhibit consistently better agreement with experiment in the vicinity of the discontinuities in streamwise surface curvature at the ogive-cylinder and cylinder-boattail junctions. At  $\alpha = 6.3^\circ$  (Figure 7) the PNS computation continues to exhibit good agreement with the experimental measurements, while the inviscid computation indicates a discrepancy on the leeward side of the boattail. The discrepancy is attributed to the strong viscous interaction caused by the appearance of crossflow separation and the roll up of leeward-side vortices in the vicinity of the boattail. As the angle of attack is increased further, the crossflow separation region extends progressively farther forward along the body. At  $\alpha = 10.4^\circ$  the PNS computation exhibits good agreement with the experimental measurements, while the inviscid results deviate from the experiment on both the leeward side of the cylinder and the boattail.

The appearance of a crossflow separation region is further indicated by the circumferential surface pressure distributions. Examples of comparisons of these distributions are shown for  $\alpha = 6.3^\circ$  in Figure 9 and for  $\alpha = 10.4^\circ$  in Figure 10 at two longitudinal stations; one on the cylinder portion of the

---

11. Schiff, L. B., "Nonlinear Aerodynamics of Bodies in Coning Motion," *AIAA Journal*, Vol. 10, No. 11, November 1972, pp. 1517-1522.

12. Sanders, B. R., and Dwyer, H. A., "Magnus Forces on Spinning Supersonic Cones, Part II: The Inviscid Flow," *AIAA Journal*, Vol. 14, No. 5, May 1976, pp. 576-582.

model near the boattail, the second, midway on the boattail. At  $\alpha = 4.2^\circ$  such comparisons (not shown) indicated uniformly good agreement between both computations and the experiment for all body stations. At  $\alpha = 6.3^\circ$  (Figure 9a) the comparison on the cylinder indicates excellent agreement between the PNS computation and experiment and the appearance of a systematic discrepancy between the inviscid computation and experiment for  $100^\circ < \phi < 150^\circ$ . This trend is accentuated for flow on the boattail (Figure 9b). The comparison shown in Figure 10 for  $\alpha = 10.4^\circ$  indicates further development of a crossflow separation for flow over the boattail and cylinder. The abrupt rise in experimental surface pressure at  $\phi \approx 90^\circ$  indicates the location of the crossflow separation point. The inviscid computation predicts a crossflow shock at  $\phi \approx 140^\circ$  which is not present in the experimental data. At this incidence the PNS computation is in only fair agreement with the experiment and suggests an upper limit of applicability of the present computational technique of  $\alpha = 6^\circ$  for this class of body shapes.

2. Skin Friction. An example of results obtained for the skin-friction coefficients are shown in Figure 11 for a fixed longitudinal station on the cylinder near the boattail, at circumferential stations around the body. Computed results for  $\alpha = 4.2^\circ$  are shown and are compared with Preston tube measurements made at that incidence. The computed skin-friction values for  $\alpha = 4.2^\circ$  are less than the experimental ones on the windward side and greater than experiment on the leeward side of the body; however, the comparison is within the expected experimental uncertainty of  $\pm 15\%$  (the error bars in Figure 11 indicate  $\pm 0.001 c_f$  which is approximately  $\pm 10\%$ ). In addition, computed results for  $\alpha = 6.3^\circ$  are shown in Figure 11 which illustrate a shift in trend of the computed skin-friction coefficient with increasing incidence. At  $\alpha = 6.3^\circ$  the minimum value of  $c_f$  is reached at  $\phi = 150^\circ$  as opposed to  $\phi = 180^\circ$  as in the  $\alpha = 4.2^\circ$  case. This is a further indication of the developing leeward-side vortical structure with increasing incidence previously shown in the pressure distributions.

3. Streamwise Velocity Profiles. A more sensitive test of the accuracy of the PNS computational technique applied to this flow is the comparison of measured and computed boundary-layer velocity profiles. Such comparisons are shown in Figures 12-16 for two longitudinal stations; station A on the cylinder near the boattail, and station B on the boattail (see Figure 5). Each figure shows the velocity profiles for a particular longitudinal station, at circumferential stations ranging from the windward to leeward ray in  $30^\circ$  increments. The nondimensional streamwise velocity components,  $u$ , are plotted versus physical distance  $y$  measured radially from the body surface in millimeters, rather than against normalized  $y/\delta$ . This method of plotting prevents scaling differences between the computation and experiment from giving a false comparison.

Comparisons for  $\alpha = 4.2^\circ$  are shown in Figure 12 for the cylinder (Station A) and in Figure 13 for the boattail (Station B). The agreement is, in general, excellent. This is particularly true on the windward side of the body. However, a slight discrepancy is visible for the profiles at  $\phi = 150^\circ$ , which is more apparent in Figure 13.

Similar comparisons for  $\alpha = 6.3^\circ$  are shown in Figures 14-15. At this angle of attack the windward side measured and computed profiles are still in excellent agreement. However, the discrepancy between the profiles at  $\phi = 150^\circ$  is substantial, particularly at the boattail station (Figure 15). Note that this discrepancy is less strongly reflected in the surface pressure distribution at the corresponding station (Figure 9b).

To assess the relative roles of circumferential pressure gradients versus the expansion over the boattail as the source of the discrepancy in the velocity profiles, a comparison was also made at  $\alpha = 6.3^\circ$  for a body with a straight cylindrical afterbody replacing the boattail. This comparison is shown in Figure 16 at a longitudinal station comparable to that of the boattail. The same computation overprediction of streamwise velocity at  $\phi = 150^\circ$  is present as well observed for the boattailed body. This result suggests that the source of the discrepancy is not flow expansion over the boattail, but rather is linked primarily to the development of the leeward-side vortex structure.

4. Circumferential Velocity. A descriptive indication of the development of the leeward-side vortex structure with increasing incidence can be seen in Figures 17-19. These figures show the projections of the computed flow velocity vectors onto the crossflow plane (i.e., a plane normal to the body axis of symmetry) located at  $x = 324\text{mm}$ , on the boattail, for angles of attack of  $4.2^\circ$ ,  $6.3^\circ$ , and  $10.4^\circ$ , respectively. At  $\alpha = 4.2^\circ$  no crossflow separation (characterized by circumferential flow from the leeward toward the windward side of the body) is observed at this longitudinal station. At  $\alpha = 6.3^\circ$  crossflow separation is observed at a crossflow separation angle,  $\phi_s$ , of  $132^\circ$ . This angle, obtained from interpolation of the computed circumferential velocity just above the body surface, is shown in Figure 18. Examination of additional longitudinal stations indicates that, at this angle of attack, the crossflow separation region starts just downstream of the cylinder-boattail junction. At  $\alpha = 10.4^\circ$  the crossflow separation angle  $\phi_s = 117^\circ$  (Figure 19), and the region of crossflow separation starts farther up the body, in the vicinity of the ogive-cylinder junction.

Experimental vapor-screen flow visualization photos<sup>13</sup> of the leeward-side vortices on the boattail are shown in Figures 20-22, at angles of attack of  $4.2^\circ$ ,  $6.3^\circ$ , and  $10.4^\circ$ . In the vapor-screen technique water vapor is introduced into the wind tunnel to produce a fog in the test section. A thin, intense plane of light, oriented normal to the body axis of symmetry at a longitudinal station midway along the boattail, illuminates the fog. The leeward-side vortices are visible as dark regions within the light plane. The growth of the vortices with increasing angle of attack is clearly visible.

Comparison of the vapor-screen photos and the computed circumferential velocity plots suggests that the computed regions of crossflow separation are

---

13. *Nietubicz, C. J., Unpublished BRL Wind Tunnel Data (private communication). 1979.*

more limited in extent than the regions of vorticity observed in the light plane. While this comparison is only qualitative, it is consistent with the previous comparisons of surface pressure and of streamwise boundary-layer velocity profiles. Although the present numerical technique allows the prediction of crossflow separation it is obvious that substantial discrepancies between the computation and experiment develop at angles of attack greater than  $6^\circ$ . The reason or reasons for this limitation are not known for certain; potential sources include the neglect of circumferential viscous terms within the thin-layer viscous model, and uncertainties in three-dimensional turbulence modeling. However, it is of interest to note that McRae and Hussaini<sup>14</sup>, who used a numerical technique which retains the circumferential viscous terms and employs a similar eddy-viscosity model in a study of turbulent cone flows at large incidence, also found significant discrepancies within the crossflow separation region. In their study, the discrepancies were reduced by modifying the eddy-viscosity turbulence model in the separated region. Rakich, et al.<sup>4</sup> reported similar behavior for flow over cones.

## V. CONCLUDING REMARKS

This report has described the results of a numerical computational study in which the parabolized Navier-Stokes marching code recently developed by Schiff and Steger has been exercised for a 6-caliber, ogive-cylinder-boattail shape at incidence. Extensive, detailed comparisons to experimental data at  $M = 3$ ,  $\alpha < 10.4^\circ$  have been performed to evaluate the accuracy and stability of the numerical technique.

Comparisons have been made showing excellent agreement between computation and experiment for surface pressures at angles of attack up to  $6.3^\circ$ . At an angle of attack of  $10.4^\circ$ , the comparison is degraded due to the inability to accurately model the significant streamwise vortical flow. Excellent agreement is also achieved for velocity profiles at  $\alpha = 4.2^\circ$ . At an angle of attack of  $6.3^\circ$ , the agreement is good with the exception of the  $\phi = 150^\circ$  circumferential station. Again, this is attributed to the inability to accurately model the developing leeward-side vortex flow. The precise cause of the inaccuracy has not been determined; however, three-dimensional turbulence modeling and inclusion of circumferential viscous terms have been identified as areas for further investigation.

Although this computation technique appears, as a result of this study, to be limited to  $\alpha < 6^\circ$  for this class of bodies, the computed results do show a significant improvement in capability compared to techniques which compute inviscid flow and viscous effects separately (see Reference 1). This increase in capability is achieved without any significant increase in computation cost or requirement for computer resources greater than those currently available with the CDC 7600 computer.

---

14. McRae, D. S., and Hussaini, M. Y., "Numerical Simulation of Supersonic Cone Flow at High Angle of Attack," AGARD-CP-247, January 1979.

## REFERENCES

1. Sturek, W. B., Dwyer, H. A., Kayser, L. D., Nietubicz, C. J., Reklis, R. P., and Opalka, K. O., "Computations of Magnus Effects for a Yawed, Spinning Body of Revolution," AIAA Journal, Vol. 16, No. 7, July 1978, pp. 687-692.
2. Lin, T. C., and Rubin, S. G., "Viscous Flow Over a Cone at Moderate Incidence: I-Hypersonic Tip Region," International Journal of Computers and Fluids, Vol. 1, 1973, pp. 37-57.
3. Lubard, S. C., and Helliwell, W. S., "Calculation of the Flow on a Cone at High Angle of Attack," AIAA Journal, Vol. 12, July 1974, pp. 965-974.
4. Rakich, J. V., Vigneron, Y. C., and Agarwal, R., "Computation of Supersonic Viscous Flows Over Ogive-Cylinders at Angle of Attack," AIAA Paper 79-0131, 17th Aerospace Sciences Meeting, January 1979.
5. Schiff, L. B., and Steger, J. L., "Numerical Simulation of Steady Supersonic Viscous Flow," AIAA Journal, Vol. 18, No. 12, December 1980, pp. 1421-1430.
6. Baldwin, B. S., and Lomax, H., "Thin Layer Approximation and Algebraic Model for Separated Turbulent Flows," AIAA Paper 78-257, 16th Aerospace Sciences Meeting, January 1978.
7. Beam, R., and Warming, R. F., "An Implicit Factored Scheme for the Compressible Navier-Stokes Equations," AIAA Journal, Vol. 16, No. 4, April 1978, pp 393-402.
8. Reklis, R. P., and Sturek, W. B., "Surface Pressure Measurements on Slender Bodies at Angle of Attack in Supersonic Flow," U.S. Army Ballistic Research Laboratory/ARRADCOM Memorandum Report ARBRL-MR-02876, Aberdeen Proving Ground, MD, November 1978. AD A064097.
9. Kayser, L. D., and Sturek, W. B., "Experimental Measurements in the Turbulent Boundary Layer of a Yawed, Spinning Ogive-Cylinder Body of Revolution at Mach 3.0. Part II. Data Tabulation," U.S. Army Ballistic Research Laboratory/ARRADCOM Memorandum Report ARBRL-MR-02813, Aberdeen Proving Ground, MD, March 1978. AD A055707.
10. Kayser, L. D., and Sturek, W. B., "Turbulent Boundary Layer Measurements on the Boattail Section of a Yawed, Spinning Projectile Shape at Mach 3.0," U.S. Army Ballistic Research Laboratory/ARRADCOM Memorandum Report ARBRL-MR-02880, Aberdeen Proving Ground, MD, November 1978. AD A065355.
11. Schiff, L. B., "Nonlinear Aerodynamics of Bodies in Coning Motion," AIAA Journal, Vol. 10, No. 11, November 1972, pp. 1517-1522.
12. Sanders, B. R., and Dwyer, H. A., "Magnus Forces on Spinning Supersonic Cones, Part II: The Inviscid Flow," AIAA Journal, Vol. 14, No. 5, May 1976, pp. 576-582.

REFERENCES (Continued)

13. Nietubicz, C. J., Unpublished BRL Wind Tunnel Data (private communication). 1979.
14. McRae, D. S., and Hussaini, M. Y., "Numerical Simulation of Supersonic Cone Flow at High Angle of Attack," AGARD-CP-247, January 1979.

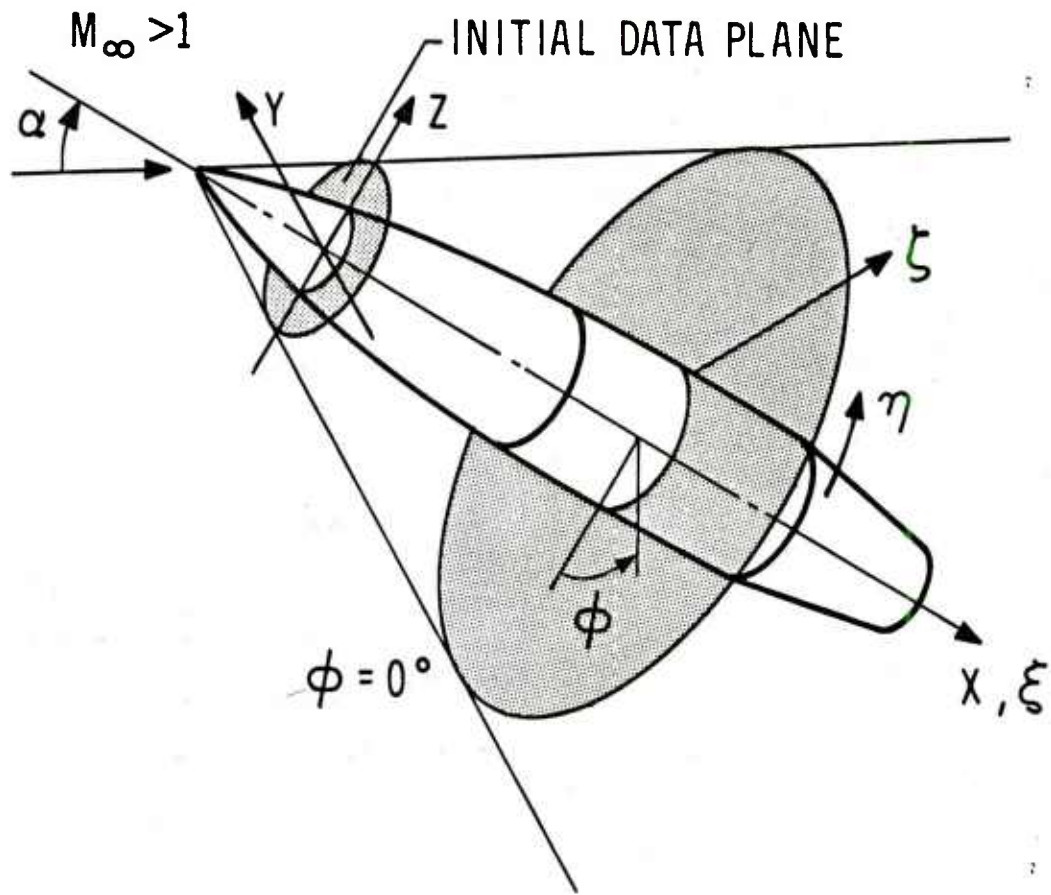


Figure 1. Coordinates and Notation

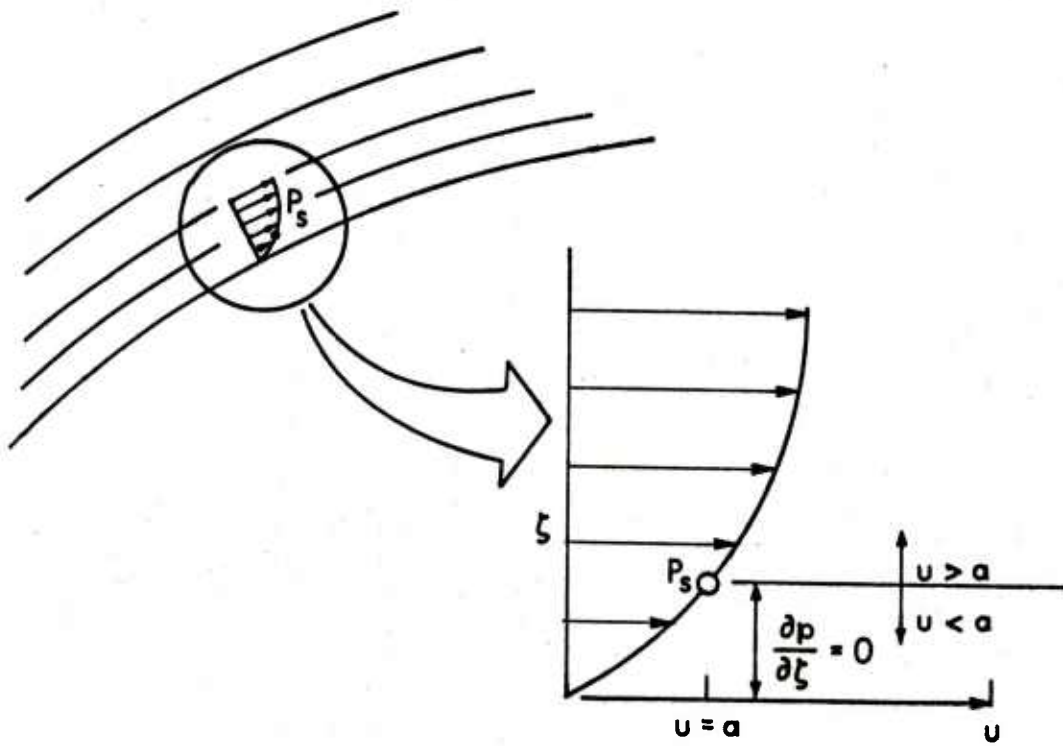


Figure 2. Subsonic Layer Approximation

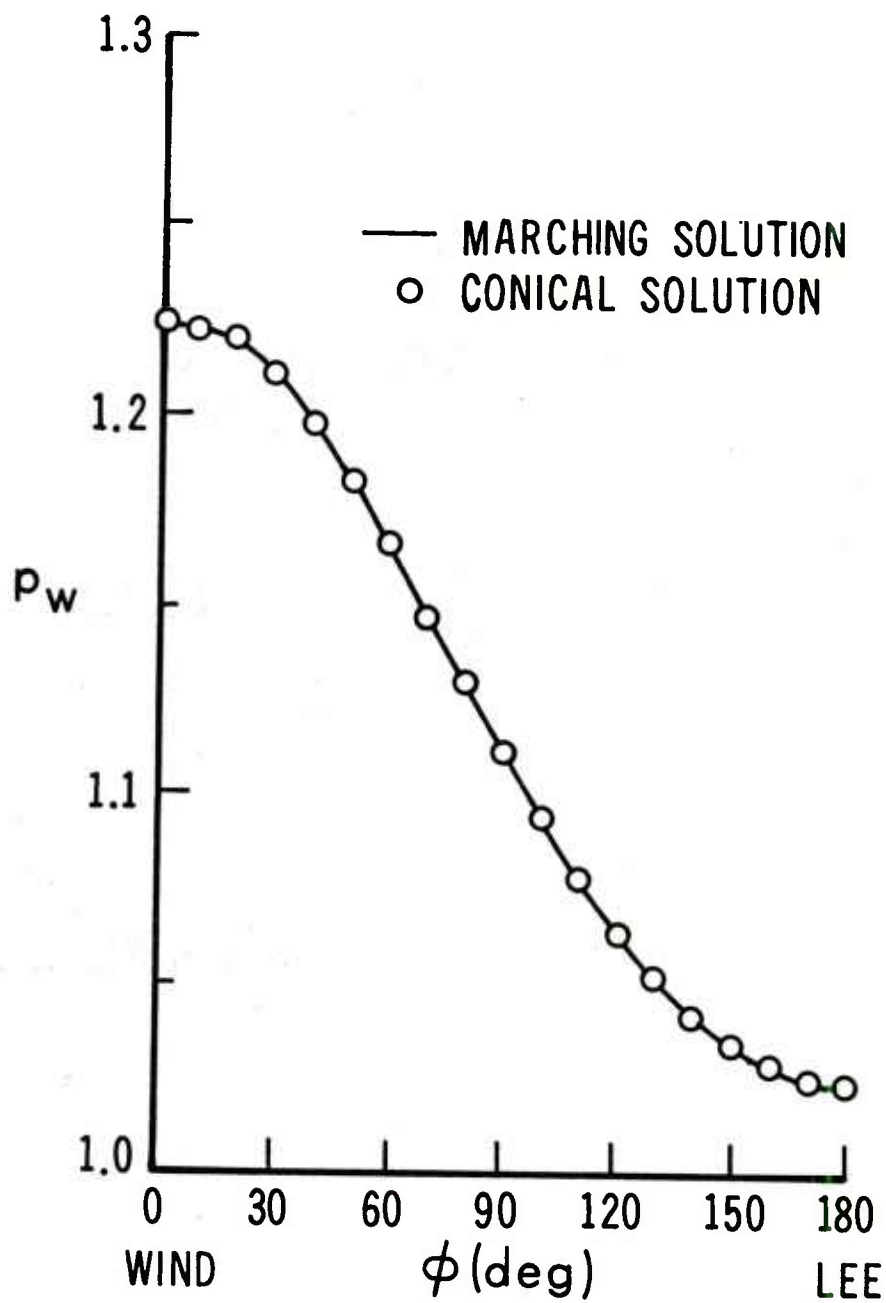


Figure 3. Circumferential Surface Pressure Distribution on  $10^\circ$  Cone;  $M = 3.0$ ,  $\alpha = 2.0$ ,  $Re_x = 1.54 \times 10^6$

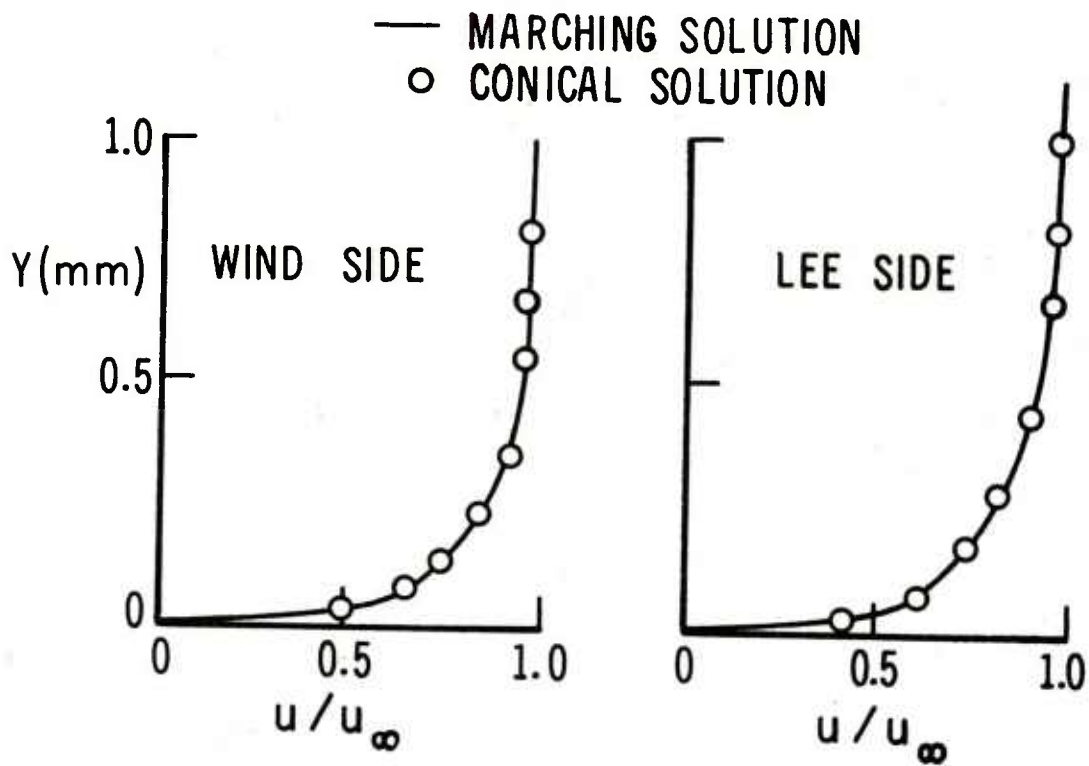
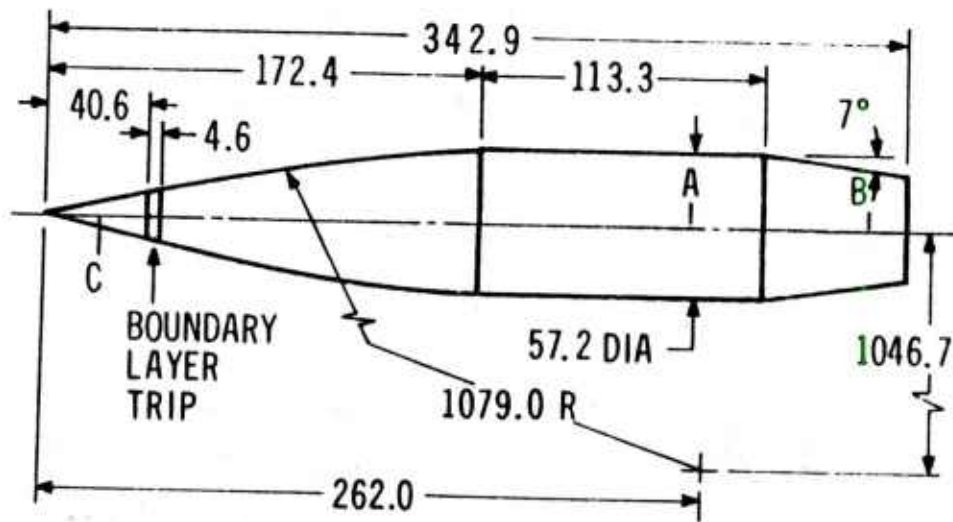


Figure 4. Windward and Leeward Boundary-Layer Velocity Profiles on  $10^\circ$  Cone;  $M = 3.0$ ,  $\alpha = 2.0$ ,  $Re_x = 1.54 \times 10^6$



NOTE: DIMENSIONS ARE IN MILLIMETRES  
 A, B BOUNDARY LAYER SURVEY STATIONS  
 C CONICAL STARTING SOLUTION STATION

Figure 5. Ogive-Cylinder-Boattail Model Dimensions

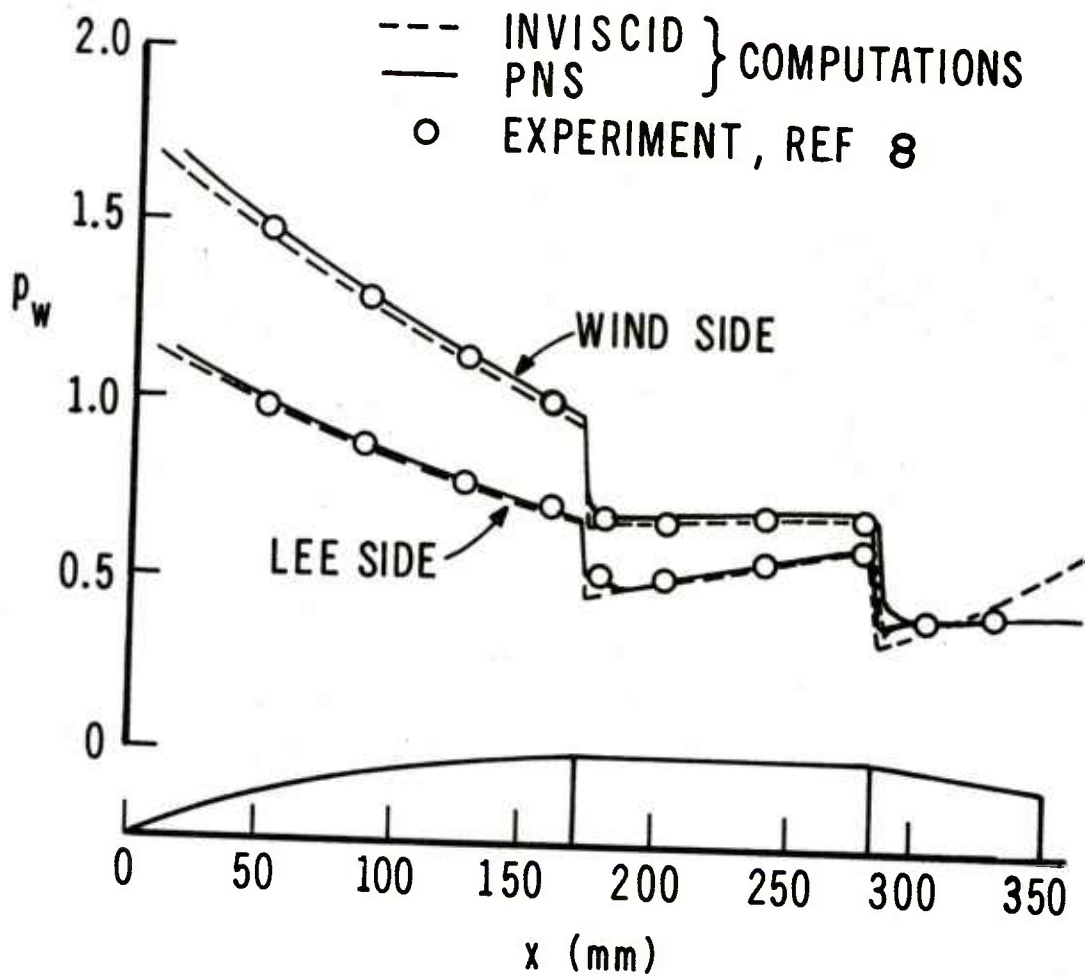


Figure 6. Axial Surface Pressure Distribution on Ogive-Cylinder-Boattail Body;  $M = 3.0$ ,  $\alpha = 4.2^\circ$ ,  $Re_\infty = 2.13 \times 10^7/m$

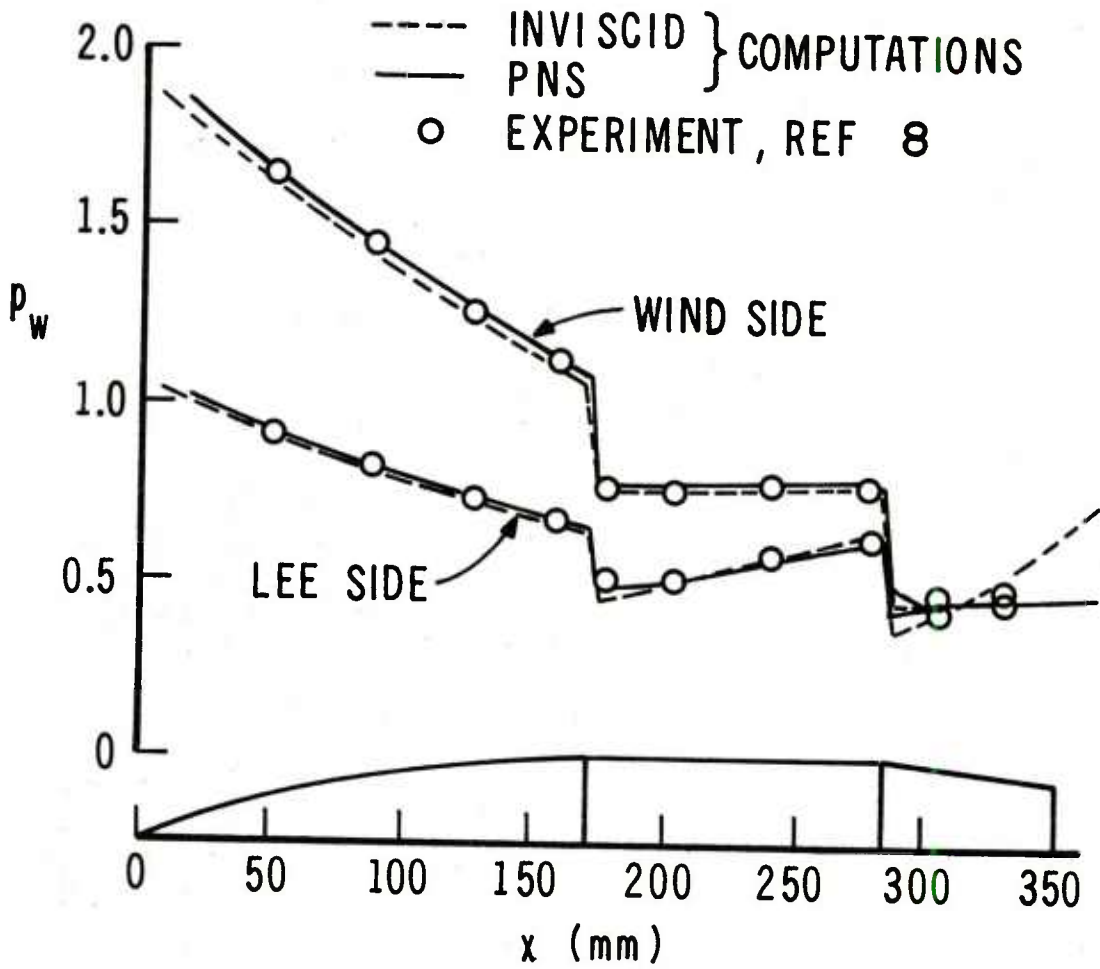


Figure 7. Axial Surface Pressure Distribution on Ogive-Cylinder-Boattail Body;  $M = 3.0$ ,  $\alpha = 6.3^\circ$ ,  $Re_\infty = 2.13 \times 10^7/m$

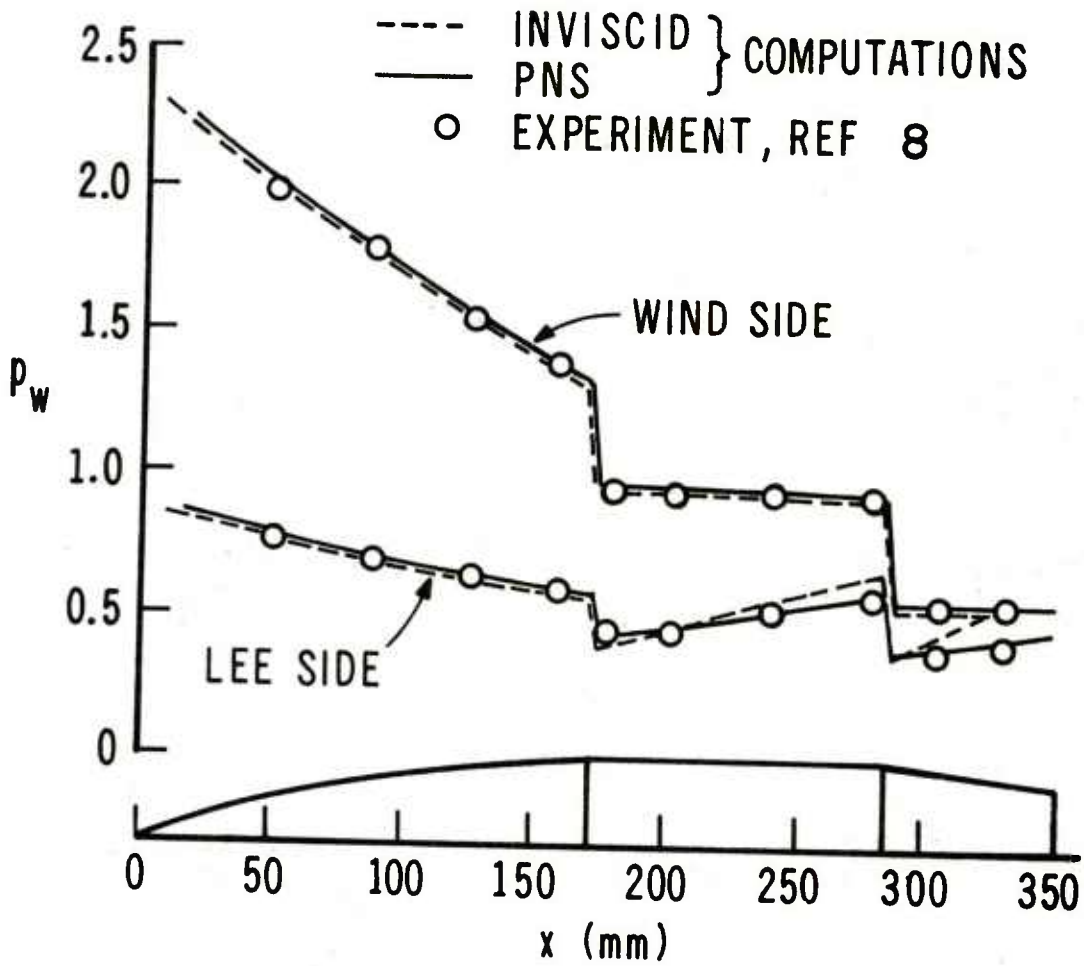


Figure 8. Axial Surface Pressure Distribution on Ogive-Cylinder-Boattail Body;  $M = 3.0$ ,  $\alpha = 10.4^\circ$ ,  $Re_\infty = 2.13 \times 10^7/m$

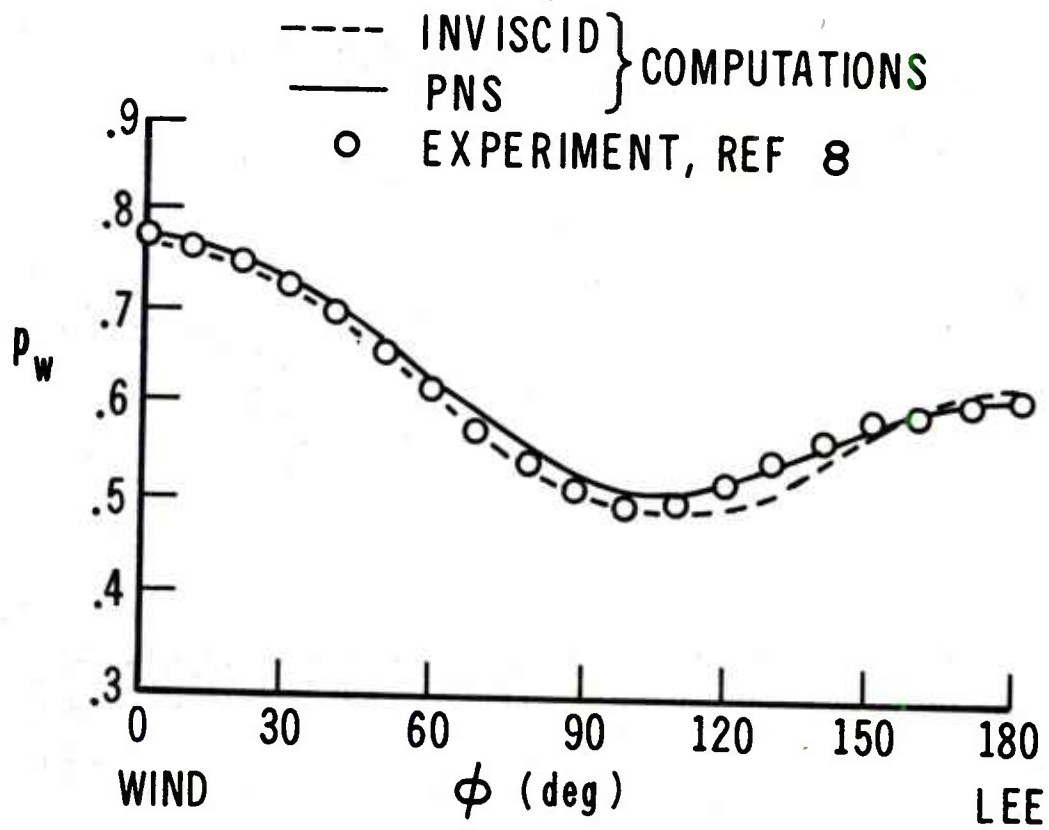


Figure 9. Circumferential Surface Pressure Distributions;  
 $M = 3.0$ ,  $\alpha = 6.3^\circ$ ,  $Re_\infty = 2.13 \times 10^6/m$

a.  $x = 279\text{mm}$  (0.915 ft), Cylinder

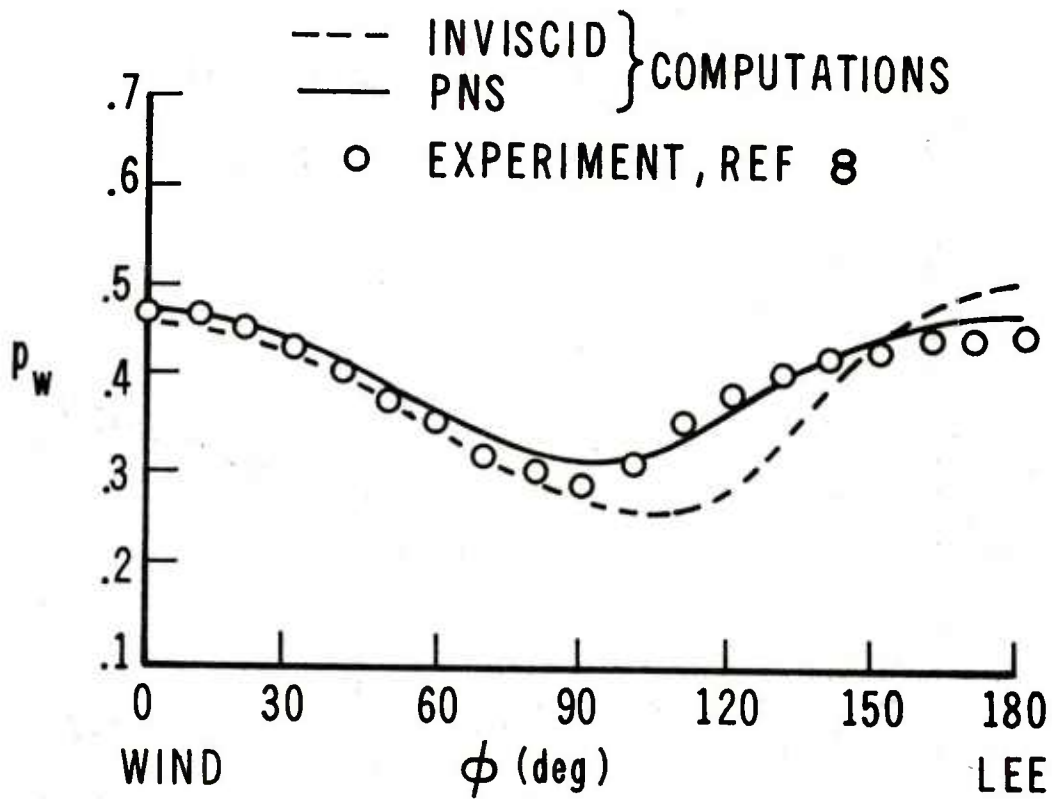


Figure 9. Circumferential Surface Pressure Distributions;  
 $M = 3.0$ ,  $\alpha = 6.3^\circ$ ,  $Re_\infty = 2.13 \times 10^6/m$

b.  $x = 330\text{mm}$  (1.082 ft), Boattail

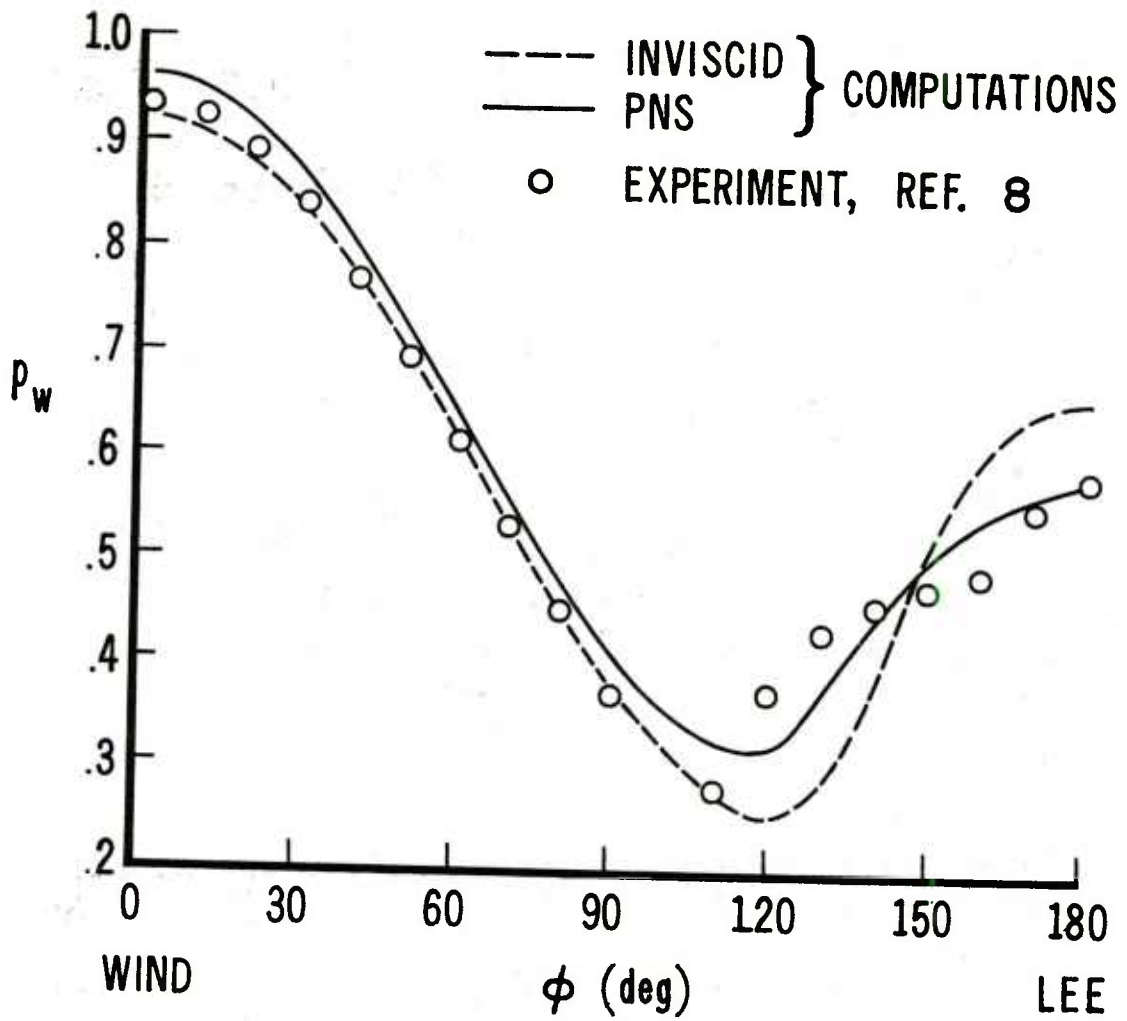


Figure 10. Circumferential Surface Pressure Distributions;  
 $M = 3.0$ ,  $\alpha = 10.4^\circ$ ,  $Re_\infty = 2.13 \times 10^6/m$

a.  $x = 279\text{mm}$  (0.915), Cylinder

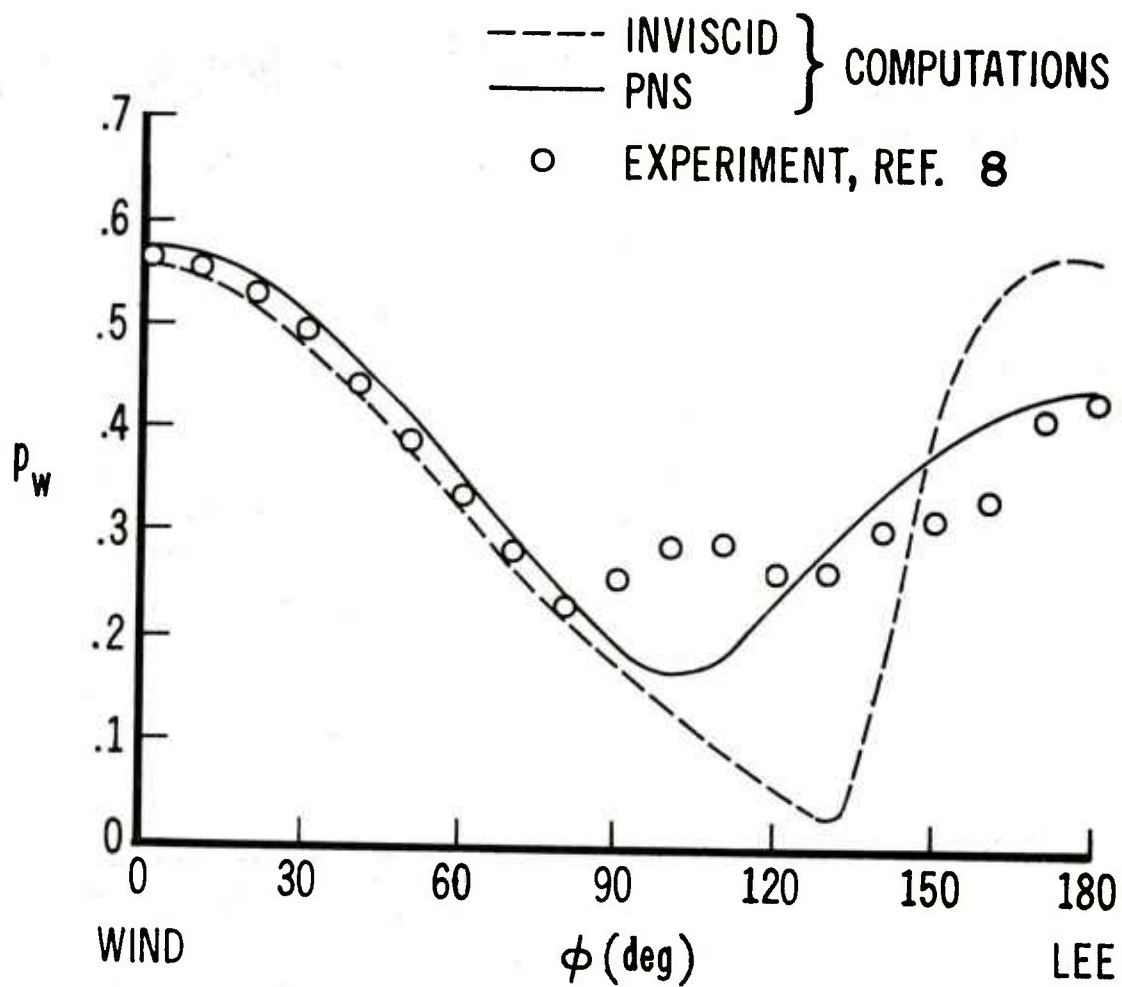


Figure 10. Circumferential Surface Pressure Distributions;  
 $M = 3.0$ ,  $\alpha = 10.4^\circ$ ,  $Re_\infty = 2.13 \times 10^6/m$

b.  $x = 330\text{mm}$  (1.082 ft), Boattail

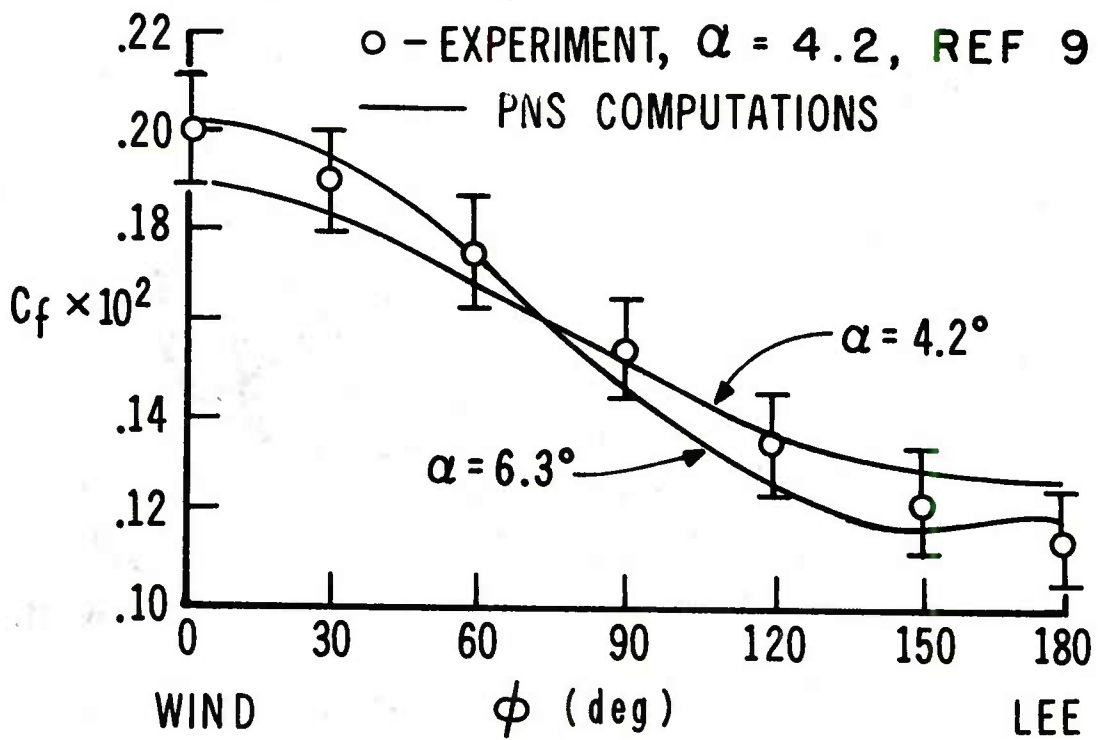


Figure 11. Circumferential Skin Friction Coefficient Distribution;  
 $M = 3.0$ ,  $x = 254\text{mm}$ ,  $Re_x = 5.41 \times 10^6$

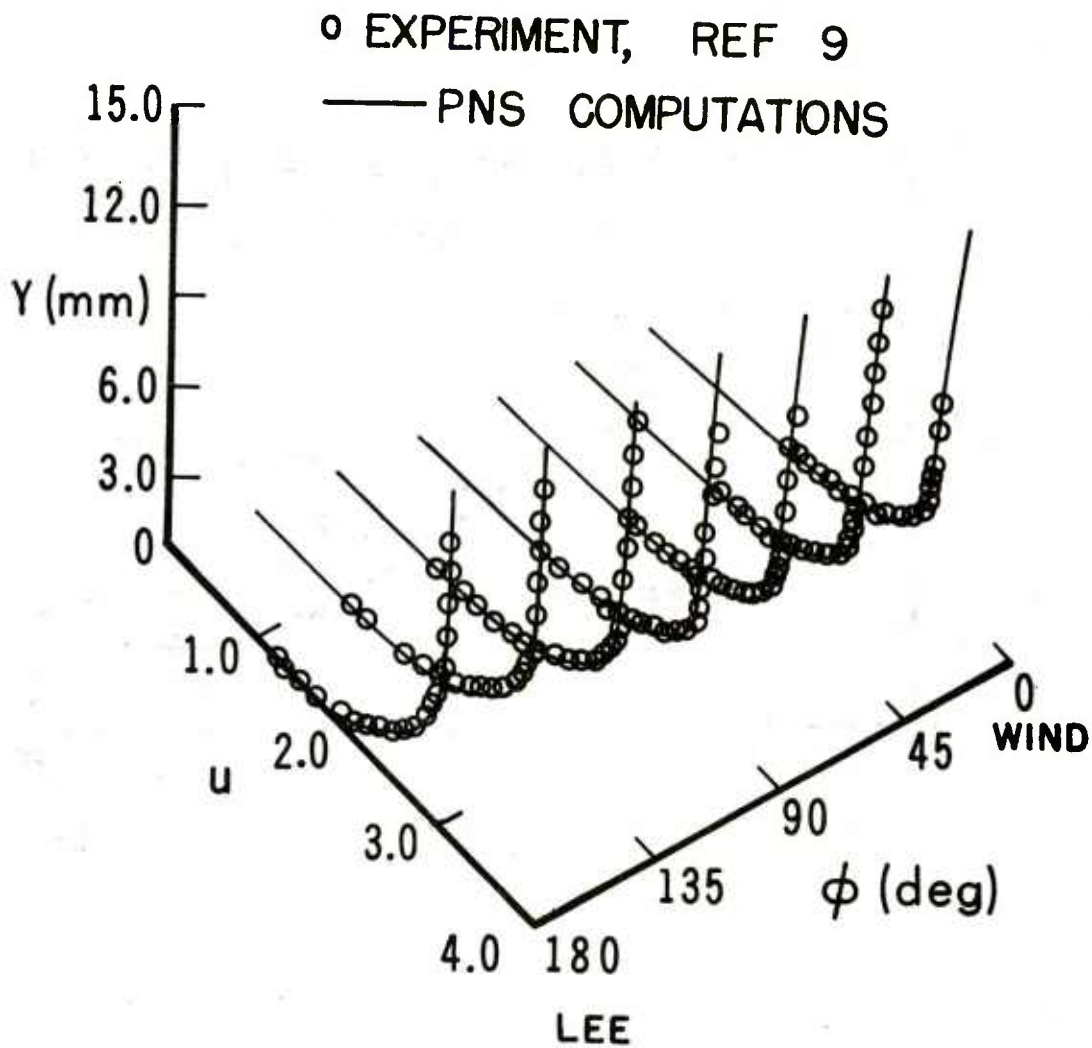


Figure 12. Boundary-Layer Velocity Profiles on Ogive-Cylinder-Boattail Body;  $M = 3.0$ ,  $\alpha = 4.2^\circ$ ,  $Re_\infty = 2.13 \times 10^7/m$ ,  $x = 254mm$  (0.833 ft), Cylinder

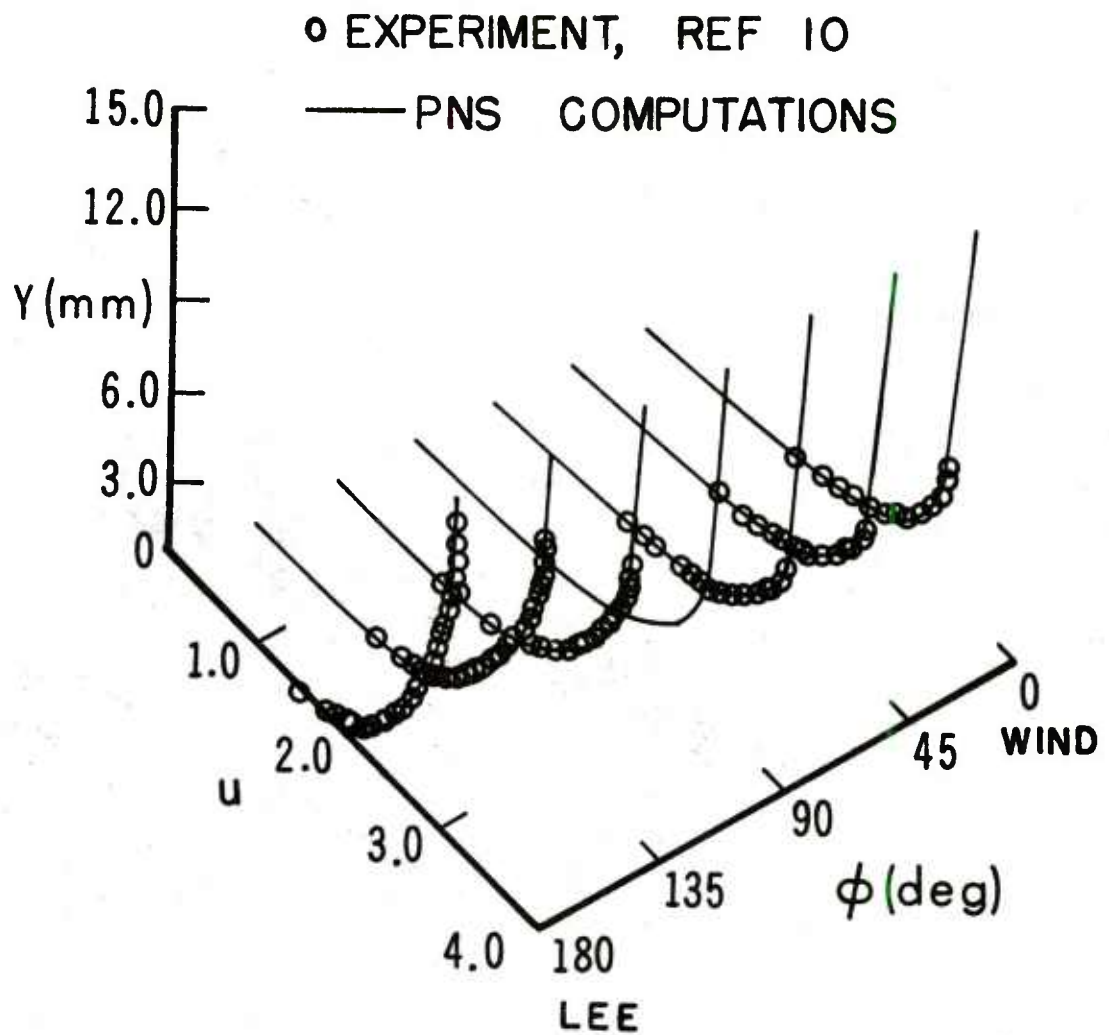


Figure 13. Boundary-Layer Velocity Profiles on Ogive-Cylinder-Boattail Body;  $M = 3.0$ ,  $\alpha = 4.2^\circ$ ,  $Re_\infty = 2.13 \times 10^7/m$ ,  $x = 324mm$  (1.063 ft), Boattail

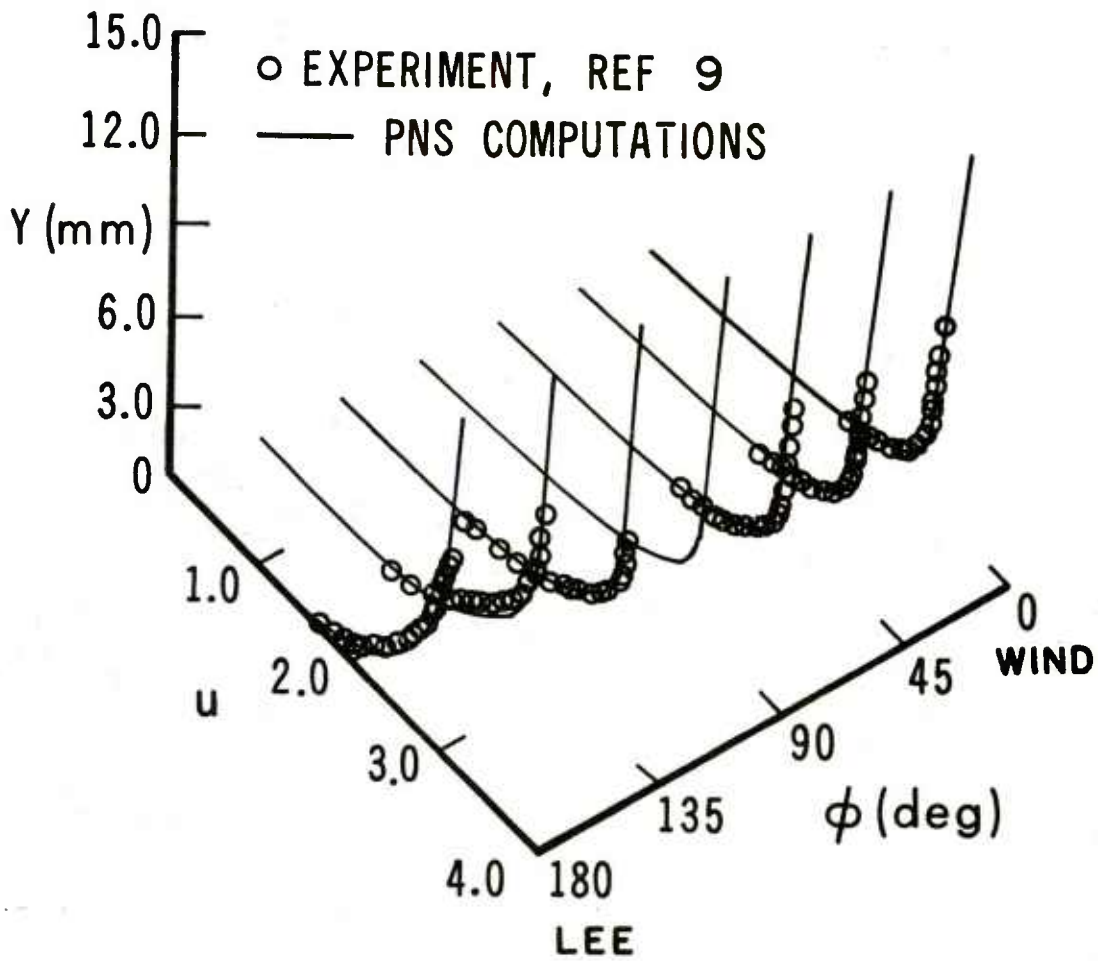


Figure 14. Boundary-Layer Velocity Profiles on Ogive-Cylinder-Boattail Body;  $M = 3.0$ ,  $\alpha = 6.3^\circ$ ;  $Re_\infty = 2.13 \times 10^7/m$ ,  $x = 254mm$  (0.833 ft), Cylinder

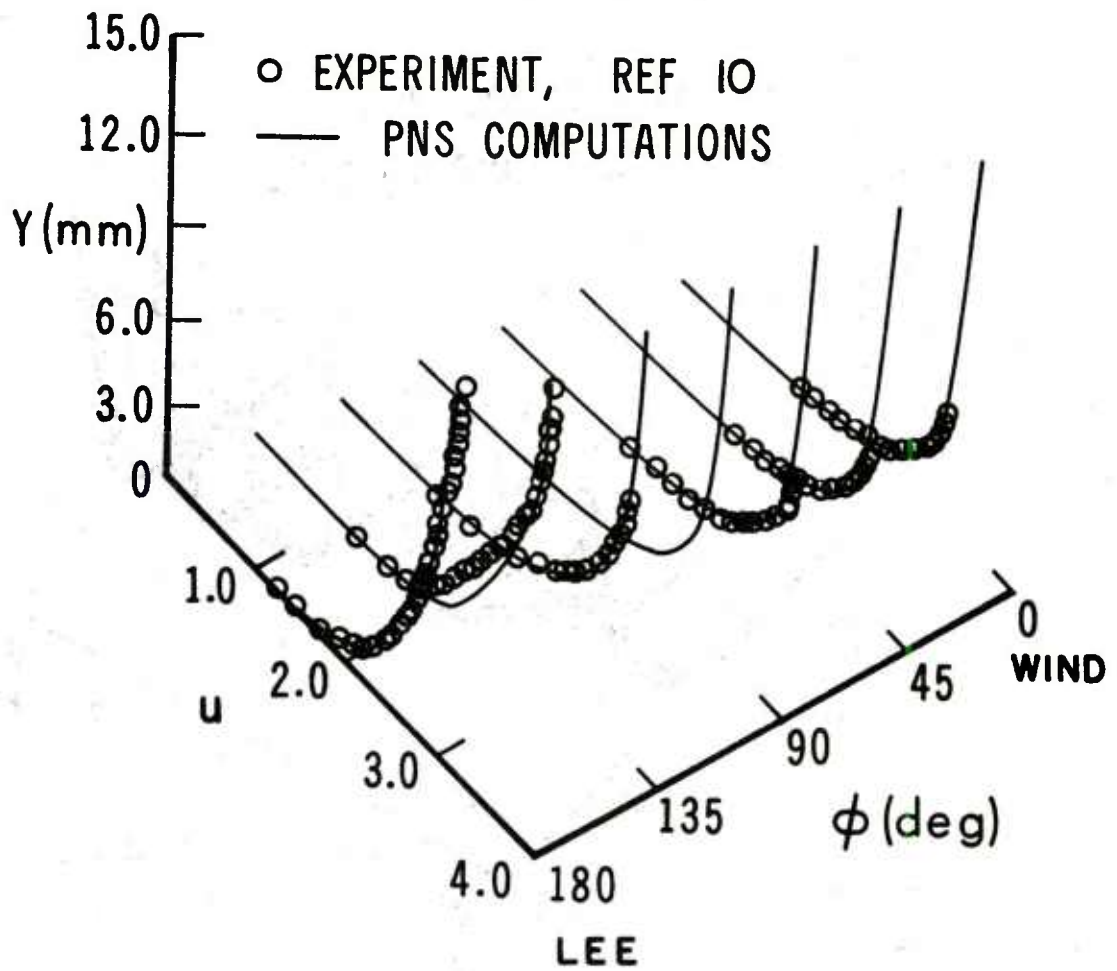


Figure 15. Boundary-Layer Velocity Profiles on Ogive-Cylinder-Boattail Body;  $M = 3.0$ ,  $\alpha = 6.3^\circ$ ,  $Re_\infty = 2.13 \times 10^7/m$ ,  $x = 324\text{mm}$  (1.063 ft), Boattail

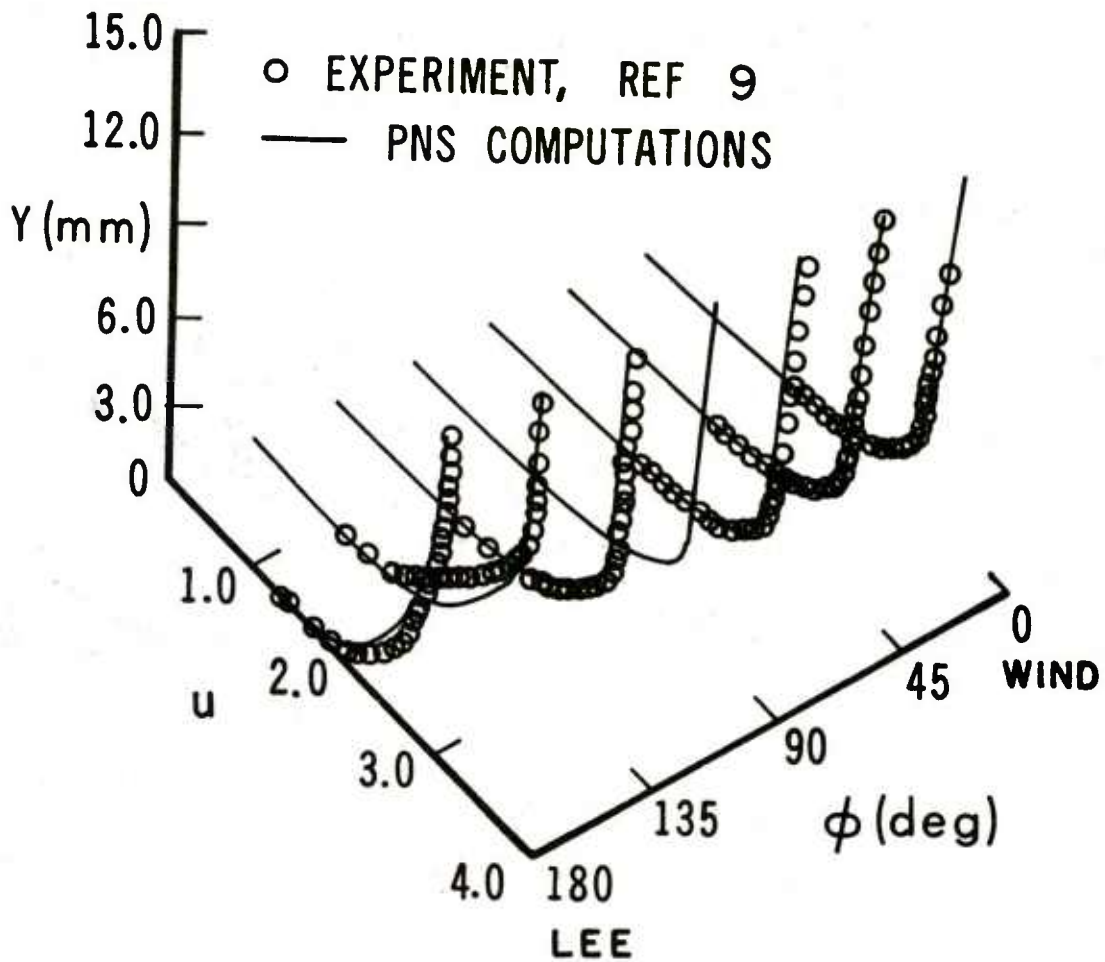


Figure 16. Boundary-Layer Velocity Profiles on Ogive-Cylinder Body;  
 $M = 3.0$ ,  $\alpha = 6.3^\circ$ ,  $Re_\infty = 2.13 \times 10^7/m$ ,  $x = 318\text{mm}$  (1.043 ft)

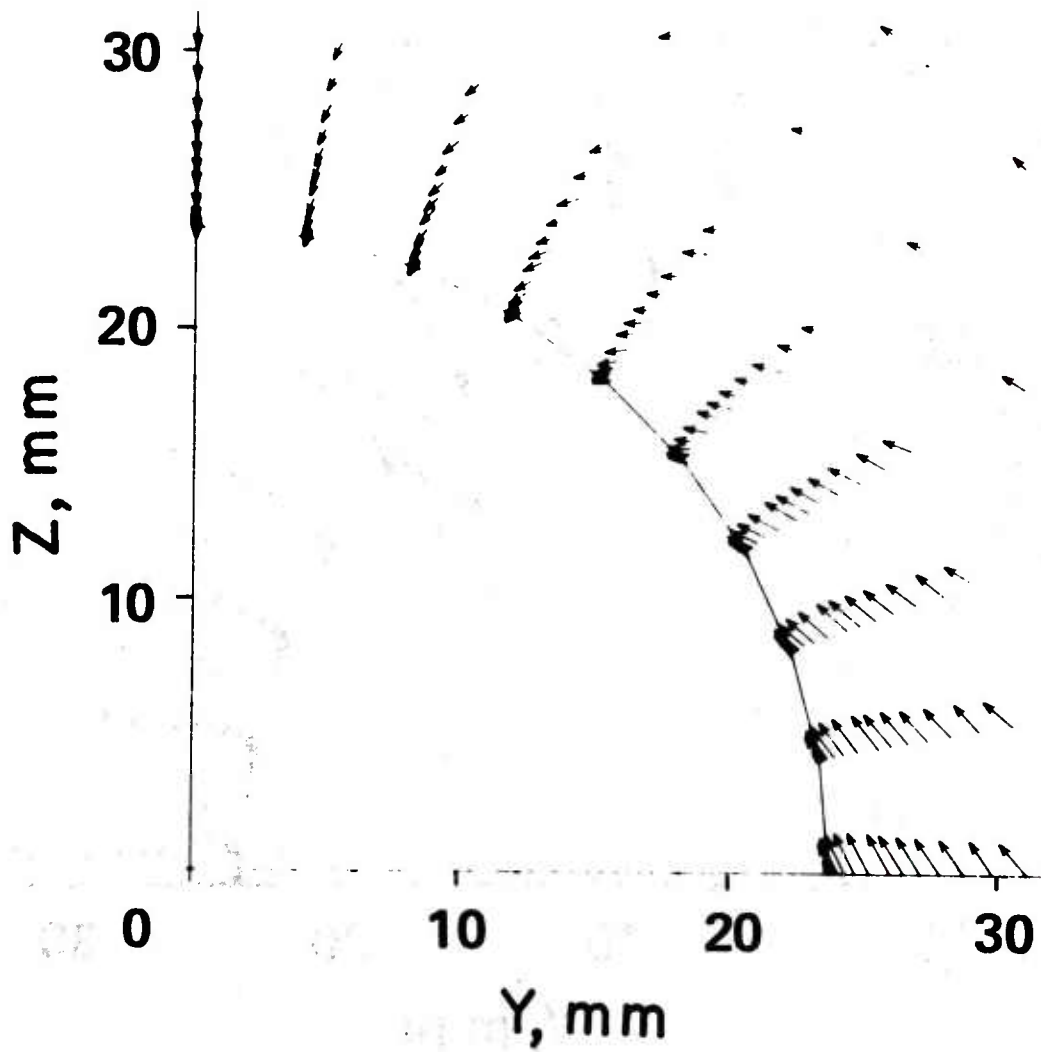


Figure 17. Crossflow Plane Velocity Vectors on Boattail;  $M = 3.0$ ,  
 $\alpha = 4.2^\circ$ ,  $Re_\infty = 2.13 \times 10^7/m$ ,  $x = 324\text{mm}$  (1.063 ft)

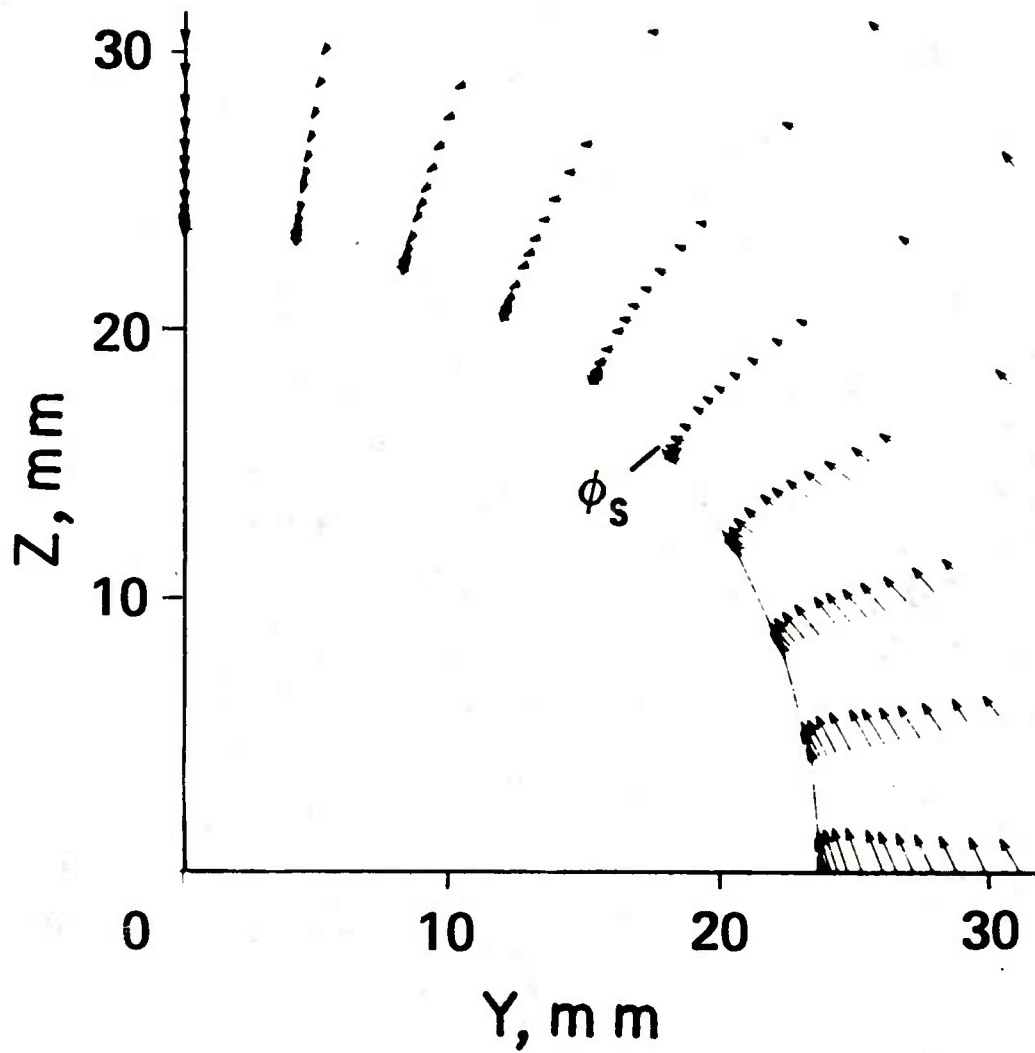


Figure 18. Crossflow Plane Velocity Vectors on Boattail;  $M = 3.0$ ,  
 $\alpha = 6.3^\circ$ ,  $Re_\infty = 2.13 \times 10^7/m$ ,  $x = 324mm$  (1.063 ft)

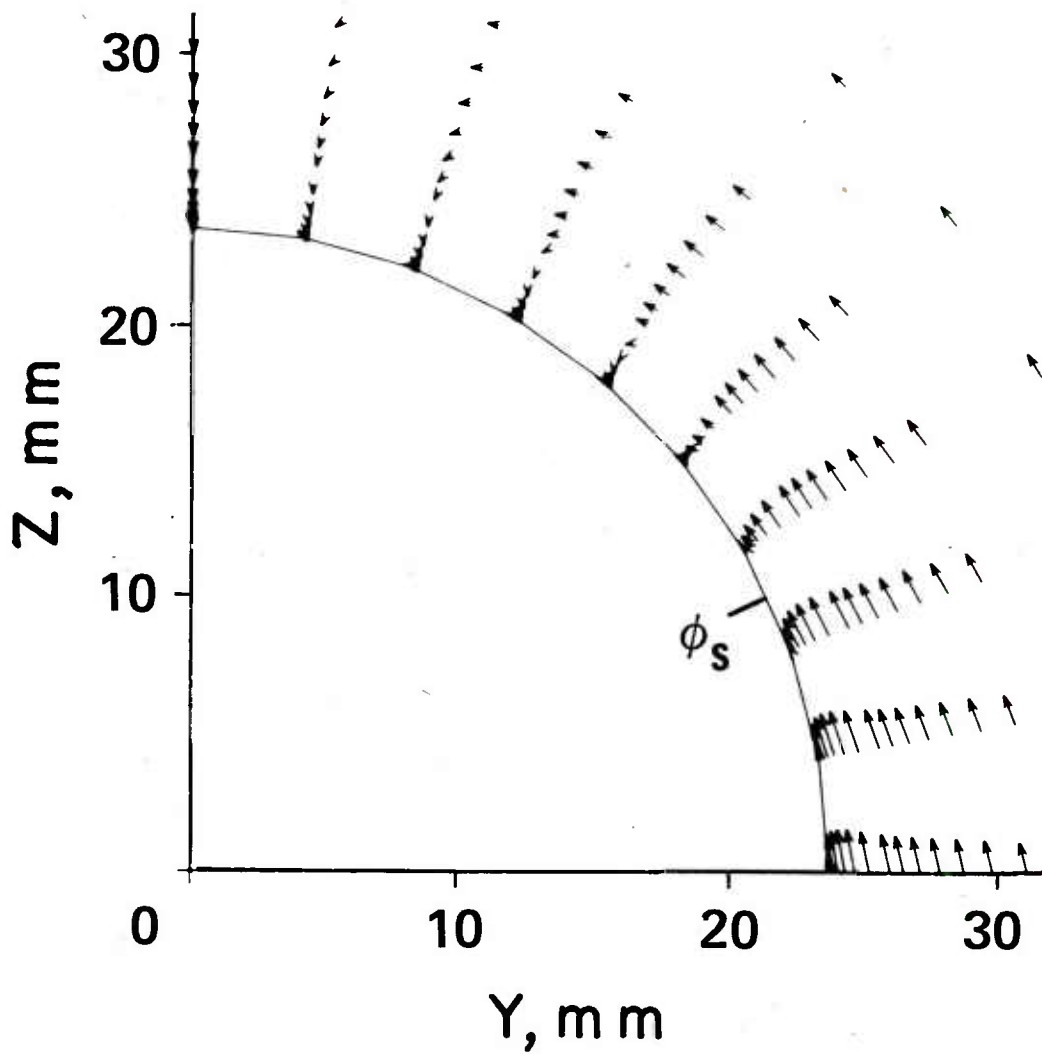


Figure 19. Crossflow Plane Velocity Vectors on Boattail;  $M = 3.0$ ,  
 $\alpha = 10.4^\circ$ ,  $Re_\infty = 2.13 \times 10^7/m$ ,  $x = 324\text{mm}$  (1.063 ft)

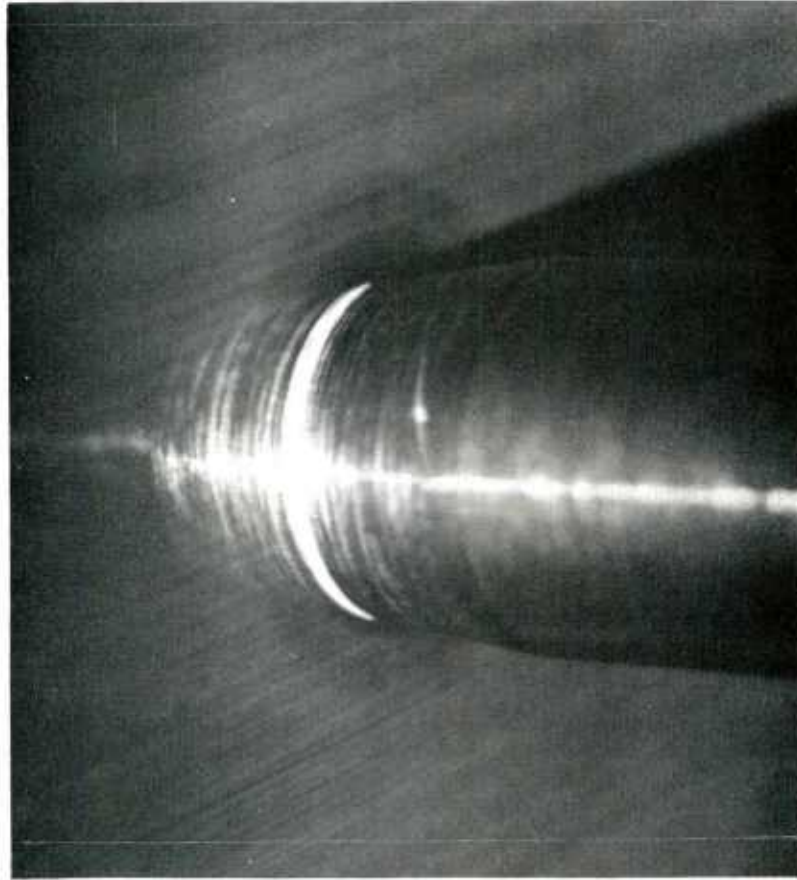


Figure 20. Vapor-Screen Flow Visualization on Boattail;  $M = 3.0$ ,  
 $\alpha = 4.2^\circ$ ,  $Re_\infty = 2.13 \times 10^7/m$

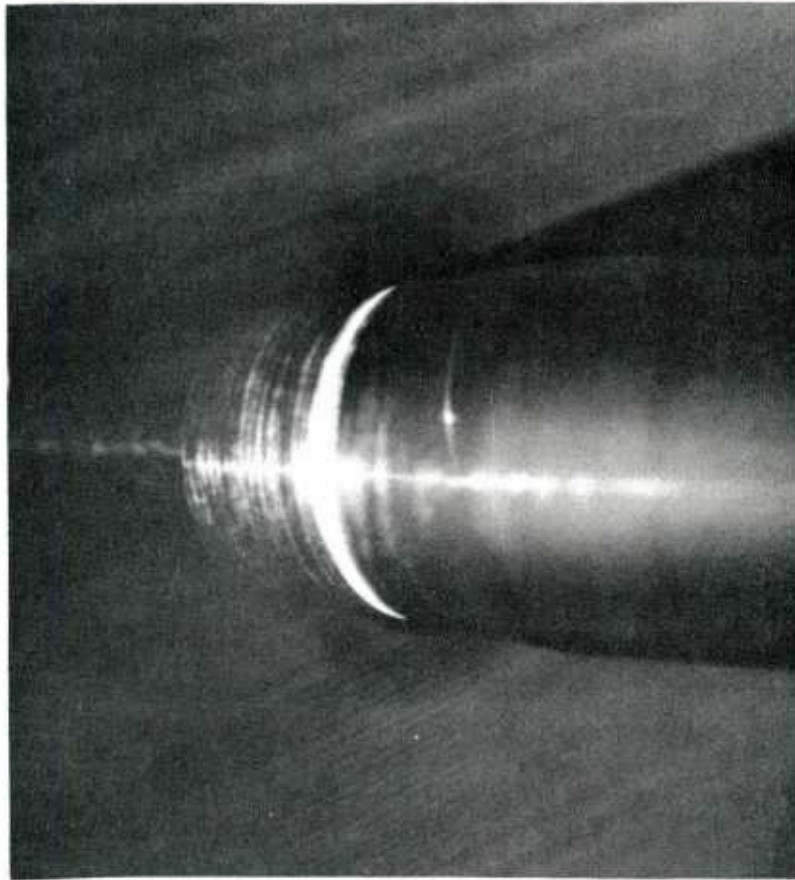


Figure 21. Vapor-Screen Flow Visualization on Boattail;  $M = 3.0$ ,  
 $\alpha = 6.3^\circ$ ,  $Re_\infty = 2.13 \times 10^7/m$



Figure 22. Vapor-Screen Flow Visualization on Boattail;  $M = 3.0$ ,  
 $\alpha = 10.4^\circ$ ,  $Re_\infty = 2.13 \times 10^7/m$

## LIST OF SYMBOLS

a	speed of sound
$c_f$	skin friction coefficient
$c_p$	specific heat at constant pressure
e	total energy per unit volume of fluid, normalized by $\rho_\infty a_\infty^2$
$e_i$	internal energy, normalized by $a_\infty^2$
$\hat{E}_s, \hat{F}, \hat{G}, \hat{q}$	flux vectors of transformed gasdynamic equation (Eq. 2)
J	Jacobian of transformation between physical and computational coordinates
L	reference length
M	Mach number
p	pressure, normalized by $\rho_\infty a_\infty^2$
Pr	Prandtl number, $\mu_\infty c_p / \kappa_\infty$
Re	Reynolds number, $\rho_\infty U_\infty L / \mu_\infty$
$\hat{R}e$	Reynolds number (Eq. 1), $\rho_\infty a_\infty L / \mu_\infty$
$\hat{S}$	viscous flux vector (Eq. 6)
u, v, w	Cartesian velocity components along the x, y, z axes, respectively, normalized by $a_\infty$
U, V, W	Contravariant velocity components (Eq. 3)
x, y, z	physical Cartesian coordinate axes (Figure 1)
$\alpha$	angle of attack
$\gamma$	ratio of specific heats
$\kappa$	coefficient of thermal conductivity, normalized by free-stream value $\kappa_\infty$
$\mu$	coefficient of viscosity, normalized by free-stream value $\mu_\infty$
$\xi, \eta, \zeta$	computational coordinates in the axial, circumferential, and radial directions (Figure 1)

LIST OF SYMBOLS (Continued)

$\rho$  density, normalized by free-stream density  $\rho_\infty$   
 $\phi$  circumferential angle (Figure 1)

Subscripts

$\infty$  free-stream conditions  
w body surface values  
x based on axial distance from nose

## DISTRIBUTION LIST

<u>No. of Copies</u>	<u>Organization</u>	<u>No. of Copies</u>	<u>Organization</u>
12	Commander Defense Technical Info Center ATTN: DDC-DDA Cameron Station Alexandria, VA 22314	1	Director US Army Air Mobility Research and Development Laboratory Ames Research Center Moffett Field, CA 94035
1	Commander US Army Materiel Development and Readiness Command ATTN: DRCDMD-ST 5001 Eisenhower Avenue Alexandria, VA 22333	1	Commander US Army Communications Research and Development Command ATTN: DRDCO-PPA-SA Fort Monmouth, NJ 07703
9	Commander US Army Armament Research and Development Command ATTN: DRDAR-TSS (2 cys) DRDAR-LCA-F Mr. D. Mertz Mr. E. Falkowski Mr. A. Loeb Mr. R. Kline Mr. S. Kahn Mr. S. Wasserman Mr. H. Hudgins Dover, NJ 07801	1	Commander US Army Electronics Research and Development Command Technical Support Activity ATTN: DELSD-L Fort Monmouth, NJ 07703
1	Commander US Army Armament Materiel Readiness Command ATTN: DR SAR-LEP-L, Tech Lib Rock Island, IL 61299	3	Commander US Army Missile Command ATTN: DRSMI-R DRSMI-RDK Mr. R. Deep Mr. R. Becht Redstone Arsenal, AL 35809
1	Director US Army Armament Research and Development Command ATTN: DRDAR-LCB-TL Watervliet, NY 12189	1	Commander US Army Missile Command ATTN: DRSMI-YDL Redstone Arsenal, AL 35809
1	Commander US Army Aviation Research and Development Command ATTN: DRDAV-E 4300 Goodfellow Blvd St. Louis, MO 63120	1	Commander US Army Tank Automotive Research and Development Command ATTN: DRDTA-UL Warren, MI 48090
		1	Director US Army TRADOC Systems Analysis Activity ATTN: ATAA-SL, Tech Lib White Sands Missile Range, NM 88002

DISTRIBUTION LIST

<u>No. of Copies</u>	<u>Organization</u>	<u>No. of Copies</u>	<u>Organization</u>
1	Commander US Army Research Office P. O. Box 12211 Research Triangle Park NC 27709	4	Director NASA Ames Research Center ATTN: MS-202A-14 Dr. P. Kutler MS-202-1, Dr. T. Pulliam MS-227-8, Dr. L. Schiff MS-202, Tech Lib Moffett Field, CA 94035
1	Commander US Naval Air Systems Command ATTN: AIR-604 Washington, D. C. 20360	1	Nielsen Engineering & Research, Inc. ATTN: Dr. S. Stahara 510 Clyde Avenue Mountain View, CA 94043
2	Commander David W. Taylor Naval Ship Research and Development Center ATTN: Dr. S. de los Santos Mr. Stanley Gottlieb Bethesda, Maryland 20084	3	Sandia Laboratories ATTN: Technical Staff, Dr. W.L. Oberkampff Aeroballistics Division 5631, G.R. Eisner H.R. Vaughn Albuquerque, NJ 87184
4	Commander US Naval Surface Weapons Center ATTN: Dr. T. Clare, Code DK20 Dr. P. Daniels Mr. D. A. Jones III Mr. L. Mason Dahlgren, VA 22448	1	Massachusetts Institute of Technology ATTN: Tech Library 77 Massachusetts Avenue Cambridge, MA 02139
2	Commander US Naval Surface Weapons Center ATTN: Code 312 Mr. R. Voisinet Mr. W. Yanta Silver Spring, MD 20910	1	Stanford University Department of Aeronautics and Astronautics ATTN: Prof. J. Steger Stanford, CA 94035
1	Commander US Naval Weapons Center ATTN: Code 3431, Tech Lib China Lake, CA 93555	1	University of California, Davis Department of Mechanical Engineering ATTN: Prof. H.A. Dwyer Davis, CA 95616
1	Director NASA Langley Research Center ATTN: NS-185, Tech Lib Langley Station Hampton, VA 23365		

## DISTRIBUTION LIST

<u>No. of Copies</u>	<u>Organization</u>
1	University of Colorado Department of Aerospace Engineering ATTN: Prof. G. Inger Boulder, CO 80309
1	University of Delaware Mechanical and Aerospace Engineering Department ATTN: Dr. J. E. Danberg Newark, DE 19711
1	University of Florida ATTN: Dr. J.E. Milton P.O. Box 1918 Eglin AFB, FL 32542
1	Virginia Polytechnic Institute and State University Department of Aerospace and Oceanic Engineering ATTN: Prof. C. Lewis Blacksburg, VA 24061
<u>Aberdeen Proving Ground</u>	
	Dir, USAMSAA ATTN: DRXSY-D DRXSY-MP, H. Cohen
	Cdr, USATECOM ATTN: DRSTE-TO-F
	Dir, USACSL, Bldg. E3516, EA ATTN: DRDAR-CLB-PA

USER EVALUATION OF REPORT

Please take a few minutes to answer the questions below; tear out this sheet, fold as indicated, staple or tape closed, and place in the mail. Your comments will provide us with information for improving future reports.

1. BRL Report Number \_\_\_\_\_

2. Does this report satisfy a need? (Comment on purpose, related project, or other area of interest for which report will be used.)

\_\_\_\_\_  
\_\_\_\_\_  
\_\_\_\_\_

3. How, specifically, is the report being used? (Information source, design data or procedure, management procedure, source of ideas, etc.) \_\_\_\_\_

\_\_\_\_\_  
\_\_\_\_\_

4. Has the information in this report led to any quantitative savings as far as man-hours/contract dollars saved, operating costs avoided, efficiencies achieved, etc.? If so, please elaborate.

\_\_\_\_\_  
\_\_\_\_\_

5. General Comments (Indicate what you think should be changed to make this report and future reports of this type more responsive to your needs, more usable, improve readability, etc.) \_\_\_\_\_

\_\_\_\_\_  
\_\_\_\_\_  
\_\_\_\_\_

6. If you would like to be contacted by the personnel who prepared this report to raise specific questions or discuss the topic, please fill in the following information.

Name: \_\_\_\_\_

Telephone Number: \_\_\_\_\_

Organization Address: \_\_\_\_\_

\_\_\_\_\_  
\_\_\_\_\_